5-2021

Ultracold Akali Collisions

Alyson T. Laskowski
Trinity University, alaskows@trinity.edu

Ultracold Akali Collisions

by

Alyson Laskowski

A thesis submitted to the Department of Physics & Astronomy at

TRINITY UNIVERSITY

in partial fulfillment of the requirements for the

Bachelor of Science in Physics

May 2021

Accepted by .....
Prof. Kelvin Cheng

Accepted by .....
Prof. Nirav Mehta

Accepted by .....
Prof. David Pooley

Accepted by .....
Prof. Orrin Shindell

Accepted by .....
Prof. Jennifer Steele, Chair

Accepted by .....
Prof. Niescja Turner

Accepted by .....
Prof. Dennis Ugolini

Ultracold Akali Collisions

by

Alyson Laskowski

Submitted to the Department of Physics & Astronomy
on 2021-Apr-16, in partial fulfillment of the
requirements for the Bachelor of Science in Physics

Abstract

The nature of the interaction between ultracold atoms is sensitive to their internuclear separation distance r. When the collision partners are far apart, they are regarded as non-interacting and the state of the system is characterized by the internal degrees of the freedom of the individual atoms, namely their respective electronic and nuclear spins. However, as r begins to diminish, the atoms start to feel a weak attractive force represented by a sum of van der Waals terms with interaction energies on the order of 10^{-6} Hartree. This attractive force grows stronger as the particles continue to move towards each other, with associated interaction energies approaching $\sim 10^{-2}$ Hartree, until r reaches a point r_e, beyond which the atoms experience a strong repulsive force because the two cannot physically be on top of each other.

Quantum defect theory (QDT) lends itself to calculations involving such systems because it exploits the natural separation of length and energy scales outlined above. In the simplest QDT approximation, two constants with respect to both field and energy, the singlet and triplet quantum defects, fully describe the short-range properties of the collision. These parameters are used to approximate the short-range reaction matrix K^{sr} with a frame transformation (FT) formula. In the long-range region, a collection of quantities that are smooth in energy and field characterize the physics. Moreover, at low collision energies, these long-range parameters behave as simple, analytic functions of energy to a good approximation. With the long-range parameters and K^{sr} in hand, the real properties of the atomic system, such as elastic cross sections, can be tabulated in a relatively few easy steps.

We used this FT approximation to describe elastic s-wave collisions of ^{6}Li, ^{7}Li, ^{23}Na, ^{39}K and ^{87}Rb atoms in which the particles enter and exit the lowest-lying interaction channel. For each, we calculated the elastic cross section as a function of magnetic field, finding that our FT method is able to reproduce the resonance features of a full coupled channels (FCC) calculation for systems where the hyperfine/Zeeman splitting of the collision channels is negligible in the area where the short- and long-range regions overlap.

Thesis Supervisor: Prof. Nirav Mehta

Acknowledgments

This thesis concludes a two-year research project and my journey through Trinity. I couldn't have completed this work without support and encouragement from many people. First and foremost, I would like to thank my advisor, Dr. Nirav Mehta. When Dr. Mehta and I began working on this project in earnest two years ago, I hadn't taken a quantum mechanics class yet and had little to no coding experience. The first few months were overwhelming—lectures on the basics of scattering theory, followed by problem sets, programming exercises, and hours of reading research articles and textbooks about two-body collisions. I felt like I had so much to learn before we could even formulate a research problem. However, during these early struggles, Dr. Mehta was always a patient and supportive presence and his determination to to understand the underpinnings of quantum defect theory inspired me to work harder and enjoy the research process. I feel immensely fortunate to have had the opportunity to study under him.

I am also grateful to the entire Physics and Astronomy Department at Trinity, including all the amazing faculty members, my fellow classmates, and the members of the Mehta research group. I would also like to thank the Murchison Research program for funding my research project over the past two summers.

Lastly, my family has been a constant source of support and encouragement throughout my academic career. In particular, I want to thank my mother and father, brother and sisters, and niece and nephews. This work is dedicated to them.

Contents

Chapter 1

Introduction

Ultracold systems, in particular alkali gases cooled to milli- or nanoKelvin temperatures, have found applications in a wide range of fields—from condensed matter physics to atomic, molecular, and optical (AMO) physics to few- and many-body physics. These systems possess an extraordinary degree of control, allowing theorists and experimentalists alike to explore a number of physical phenomena and investigate fundamental properties of quantum matter. For example, in the late 1990's advancements in cooling technologies, such as laser- [38] or evaporative [30] cooling and magnetic or optical trapping, allowed for the attainment of Bose-Einstein condensates (BECs) in vapors of ^{87}Rb [1], ^{7}Li [6], and ^{23}Na [12] atoms and degenerate atomic Fermi gases of ^{40}K [13] and ^{6}Li [47] [54]. In all of these breakthroughs, Fano-Feshbach resonances were the essential tool that allowed experimentalists to control the interactions between atoms [10] and thus, it is important that the properties of these features are known to a considerable degree.

Here we develop and assess the success of a numerical method for predicting the number, positions, and widths of Fano-Feshbach resonances in alkali collisions based on multichannel quantum defect theory (MQDT) with the addition of an energy-independent frame transformation to approximate the short-range reaction matrix K^{sr}. In Chapter 2, we outline the theoretical background of quantum scattering, focusing on low-energy, two-body s-wave collisions and covering key concepts such as collision or dissociation channels, Fano-Feshbach resonances, and the total elastic cross section. Then, in Chapter 3, we discuss the properties of ultracold alkali collisions, the components of the total interaction potential, and what quantum numbers are conserved. Next, in Chapter 4, we describe our MQDT-FT approximation in detail, applying the method first to a single-channel collision of ^{7}Li atoms, then a series of multichannel problems for various alkali atoms, including ^{6}Li, ^{23}Na, ^{39}K, ^{87}Rb and ^{85}Rb. We compare our results to a full coupled-channels (FCC) calculation and analyze how well our MQDT-FT method is able to reproduce the resonance features in each collision. Lastly, in Chapter 5, we summarize our results and offer recommendations for future projects.

Chapter 2

Scattering in the Quantum Picture

In classical mechanics, collisions, like the one depicted in Figure 2-1, between two particles are completely determined by their velocities and impact parameter b, that is the distance at which they would pass by each other if they did not interact.

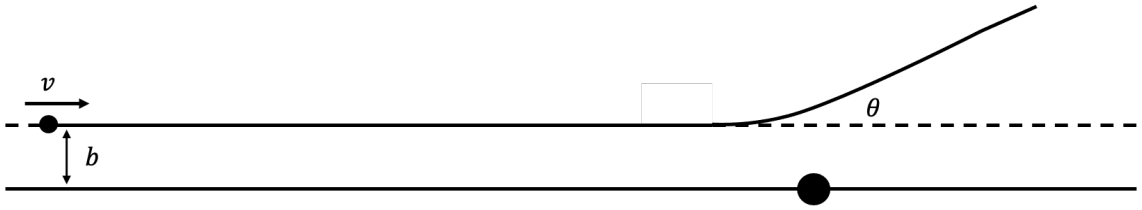

Figure 2-1: A "classical" collision in which a lighter, smaller particle with velocity v is scattered off at an angle θ after colliding with a larger, heavier particle that is initially at rest.

However, in quantum mechanics, the Heisenberg uncertainty principle eliminates any notion of definite velocities or distances such as impact parameters. Instead, the idea is to determine the likelihood that a collision will occur, and if so, the probability that the particles will scatter through a particular angle. In the following discussion we will only be covering elastic collisions in which the particles' internal quantum states are left unchanged after the interaction.

The time independent Schrodinger equation for a two-body collision is given by,

$$\Big[-\frac{\hbar^2}{2m_1}\nabla_1^2 - \frac{\hbar^2}{2m_2}\nabla_2^2 + V(r_1, r_2)\Big]\psi(r_1, r_2) = E\psi(r_1, r_2) \tag{2.1}$$

where m_1, m_2 are the masses of the particles and $V(r_1, r_2)$ is the interaction between them. $V(r_1, r_2)$ is assumed to be only a function of the internuclear separation distance $r = r_1 - r_2$ between the two colliding bodies and to be spherically symmetric. As a result, we can separate Eq. (2.1) into a set of two uncoupled Schrodinger equations,

$$\begin{aligned} \Big[-\frac{\hbar^2}{2\mu}\nabla_r^2 + V(r)\Big]\psi_{rel}(r) &= E_{rel}\psi_{rel}(r) \\ -\frac{\hbar^2}{2M}\nabla_R^2\psi_{CM}(R) &= E_{CM}\psi_{CM}(R) \end{aligned} \tag{2.2}$$

The first of these describes the motion of a relative particle of the reduced mass $\mu = \frac{m_1 m_2}{m_1+m_2}$ in a potential $V(r)$, while the second characterizes the motion the center of mass of the system where $M = m_1 + m_2$ is the total mass and $R = \frac{m_1 r_1 + m_2 r_2}{M}$ is the center of mass. Moreover, the second expression of Eq. (2.2) can be neglected if we elect to work in the reference frame of the center of mass. Thus, our two-body collision problem amounts to solving a single time-independent Schrodinger equation,

$$-\frac{\hbar^2}{2\mu}\nabla^2\psi + V(r)\psi(r) = E\psi(r). \tag{2.3}$$

for a single particle of mass μ in a spherically symmetric potential $V(r)$. Here $-\frac{\hbar^2}{2\mu}\nabla^2 = \frac{1}{r^2}\frac{\partial}{\partial r}(r^2\frac{\partial}{\partial r}) + \frac{L^2}{2\mu r}$ where L^2 is the orbital angular momentum operator. In this newly reduced problem, we envision that the relative particle is initially described as a plane wave, $\psi(z) = Ae^{ikz}$, traveling along the z-axis, as shown in Figure 2-2 [23].

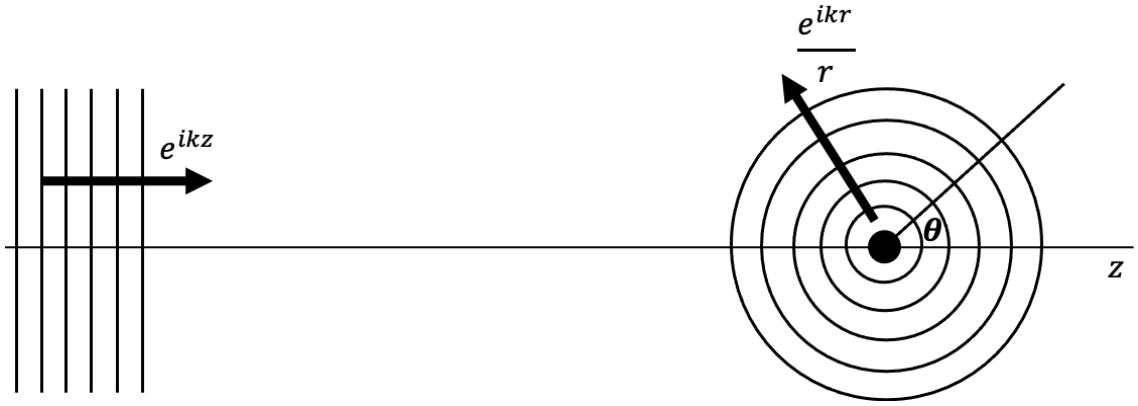

Figure 2-2: A plane wave of form e^{ikz} is incident on a symmetric scattering potential resulting in a outgoing spherical wave e^{ikr}/r.

This plane wave encounters a centrally symmetric scattering potential, resulting in an outgoing spherical wave $\psi(r) = Af(\theta)\frac{e^{ikr}}{r}$. Solutions of Eq. (2.3), therefore, must approach

$$\psi(r) \xrightarrow[r\to\infty]{} A\left[e^{ikz} + f(\theta)\frac{e^{ikr}}{r}\right] \tag{2.4}$$

at large distances. The scattering amplitude $f(\theta)$ is related to the likelihood that the particle pass through $V(r)$ will scatter at a given angle θ [23]. By calculating the probability currents of the incident plane wave j_{inc},

$$\begin{aligned} P_{inc} &= j_{inc}d\sigma \\ &= \frac{\hbar k}{m}|A|^2 d\sigma \end{aligned} \tag{2.5}$$

and outgoing spherical wave j_{out},

$$\begin{aligned} P_{out} &= j_{out}d\sigma \\ &= \frac{\hbar k}{m}\frac{|A|^2|f|^2}{r^2}r^2 d\Omega \end{aligned} \tag{2.6}$$

and requiring that $P_{inc} = P_{out}$, we arrive at the following expression for the effective cross-section, or just the cross-section of the collision,

$$d\sigma = |f(\theta)|^2 d\Omega \tag{2.7}$$

where $d\Omega$ is an element of solid angle [34].This equation is also of interest to experimentalists, since it gives the number of particles arriving at a detector spanning solid angle $d\Omega$ per unit time in terms of the incident flux of particles in the beam. Integrating this expression, the total elastic cross-section is

$$\sigma = \int |f(\theta)|^2 d\Omega. \tag{2.8}$$

This is the quantity that is of interest to experimentalists because it reflects the likelihood that a collision will occur, and the problem now becomes calculating the scattering amplitudes $f(\theta)$.

Figure 2-3 schematically illustrates the behavior of the scattering potential $V(r)$ as the separation distance r between the atoms changes. In the language of atomic physics, we say that the curve, $V(r)$, represents an interaction or collision channel which is available to the system. At very large r, the channel approaches a constant energy or threshold which corresponds to a specific combination of the internal states of the well-separated (and thus, non-interacting) atoms. The internal states of an atom, as will be discussed in Chapter 3, are related to its nuclear and electronic spins and depend on whether any external magnetic or electric fields are applied to the system, which cause the energy levels/thresholds to shift.

If the threshold energy of the channel is less than the energy of the system, as E_1 is in Figure 2-4, then the channel is said to be energetically accessible, or open to the system, while if the reverse is true—i.e., the threshold is greater than the energy—then the channel is closed. As r begins to decrease, the atoms begin to interact and the interaction is characterized by a weak attractive force which draws the bodies nearer to each other. This attractive force grows stronger with decreasing r until the particles reach a minimum separation distance r_e, beyond which the collision partners experience a strong repulsive force which causes the two to separate. This strong, short-range interaction is indicated by a deep potential well in Figure 2-3, which supports a number of bound states.

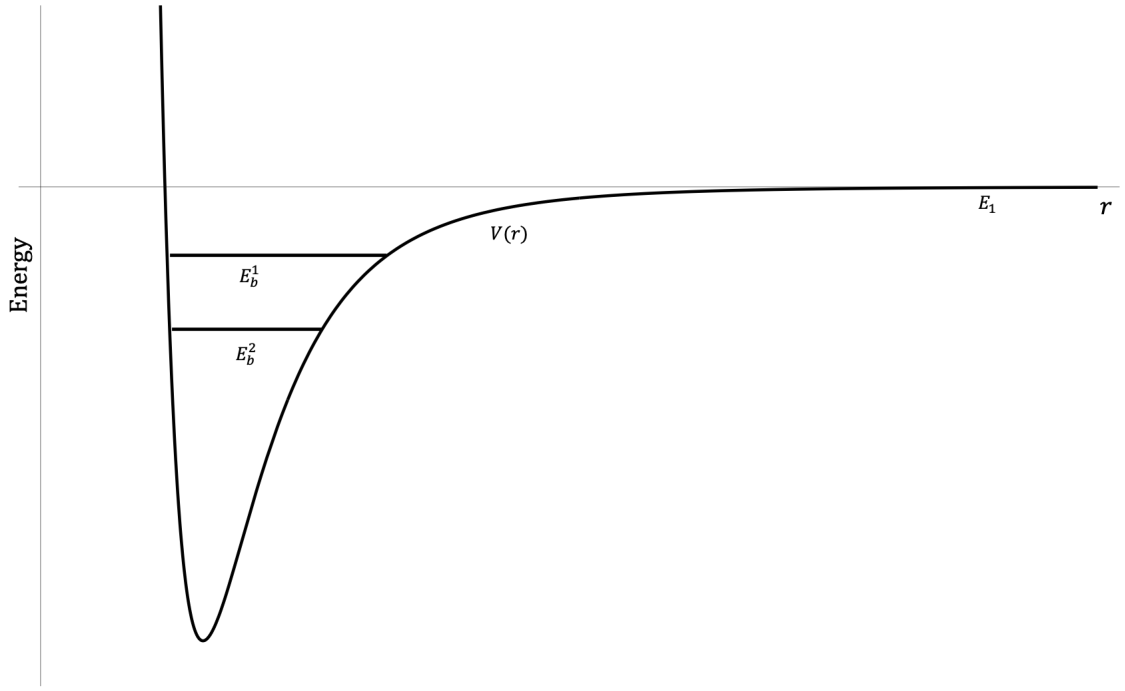

Figure 2-3: Schematic representation interaction channel $V(r)$ for a two-body collision. At large r, $V(r)$ approaches a constant energy E_1, while at very small r, it is characterized by a deep, attractive well which supports bound states E_b^1 and E_b^2.

In some atomic collisions, multiple interaction channels may be "coupled" together so that more than one channel is available to the system as depicted schematically in Figure 2-4. Here, there are two interaction channels, each defined by a different combination of the internal states of the atoms at large r and approaching a different threshold as $r \to \infty$. One of these, the lowest channel, is open, while the other is energetically inaccessible to the system. This means that the atoms will "enter" and "exit" the collision in the lowest channel, indicated as $V_1(r)$ in Figure 2-4. This type of collision is said to be elastic because the particles return to their initial internal states (if the atoms exited in a different channel than they entered in the collision is said to be inelastic). However, the latter channel supports of a number of bound states at small r, with energies E^{bound}. If one of these energies is near the threshold of the entrance/exit channel, as E_b is to E_1 in Figure 2-4, then that bound state will be accessible to the system at small separation distances r, and the atoms will form an unstable molecule temporarily, before dissociating and exiting the collision back out $V_1(r)$. This phenomenon is called a Fano-Feshbach resonance [17].

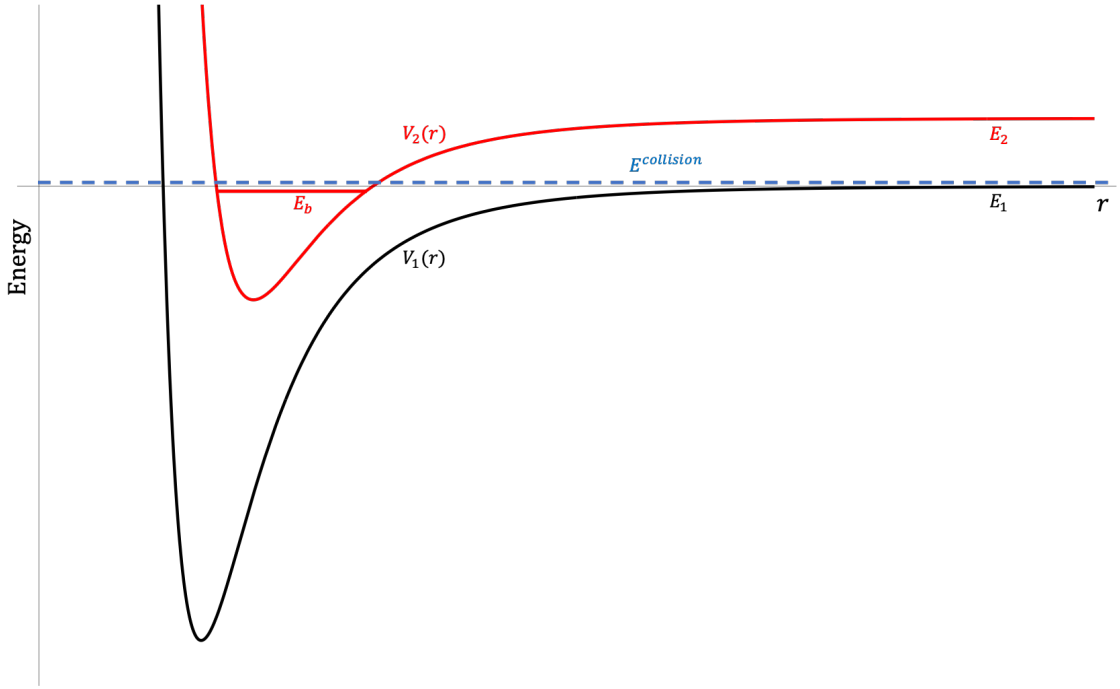

Figure 2-4: Two channel collision; when the the collision threshold is at zero, $E = E^{collision}$. The lowest channel $V_1(r)$ is open since $E_1 < E$, while $V_2(2)$ is closed because $E_2 > E$. Thus, the atoms must enter and exit the collision in quantum states corresponding to $V_1(r)$.

If the atoms are placed in an uniform magnetic field with magnitude B, then the energy thresholds will shift, causing the interior bound states to shift as well. This means that, if the collision energy is kept at a constant just above the threshold of the lowest channel E_1, Fano-Feshbach resonances will occur at the values of field when one of the bound state energies crosses E_1.

The succeeding sections briefly cover the mathematical formalism underlying the theory of quantum scattering. First, we begin by considering single-channel, two-body collisions, covering concepts such as the scattering phase shift, scattering length, and elastic cross section. Then we generalize these results for multichannel problems and discuss how the number, positions, and widths of Fano-Feshbach resonances are calculated.

2.1 Single-Channel Scattering Theory

In order to calculate the elastic cross-section σ in Eq. (2.8) for a single channel problem, we need to determine the scattering amplitudes $f(\theta)$ by solving Eq. (2.3) and matching the solution to Eq. (2.4). The following is a brief outline of this calculation and a more in-depth analysis can be found in refs.[34], [23], or [53]. Because $V(r)$ is assumed to be spherically symmetric, the solution $\psi(r)$ to Eq. (2.3) can be represented as a superposition of wavefunctions with different values of orbital angular momentum l,

$$\psi(r) = \sum_{l=0}^{\infty} A_l P_l(\cos\theta) R_l(r) \tag{2.9}$$

where A_l are constants, $P_l(\cos\theta)$ is the l^{th} Legendre polynomial, and $R_l(r)$ are radial functions [34]. The coefficients A_l are by requiring that $\psi(r)$ asymptotically approaches Eq. (2.4) and are given by,

$$A_l = \frac{1}{2k}(2l+1)i^l e^{i\delta_l} \tag{2.10}$$

where $k = \frac{\sqrt{2\mu E}}{\hbar}$ is the wavenumber and δ_l is the phase shift that the functions $R_l(r)$ accumulate in $V(r)$ [34]. Figure 2-5 shows how much phase the wavefunction accumulates in a square well potential,

$$V^{sqr}(r) = \begin{cases} -V_0, & r < r_0 \\ 0, & r \geq r_0 \end{cases} \tag{2.11}$$

where V_0 is the depth of the well and r_0 is the width of the well.

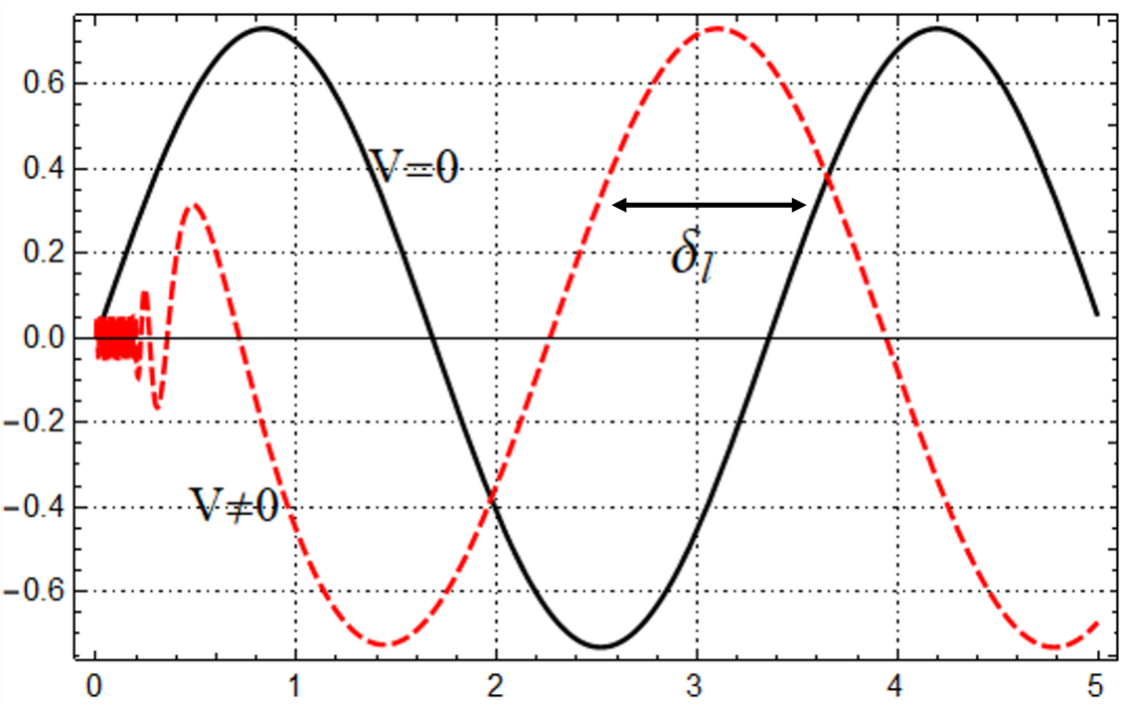

Figure 2-5: Wavefunctions $\psi(r)$ for $V(r) = 0$ (black curve) and $V(r) = V^{sqr}(r)$ (red curve). In the presence of a potential at small r, $\psi(r)$ accumulates phase because the kinetic energy is greater and therefore, the wavelength is smaller. This causes the wavefunction to differ by an amount δ_l at large r.

Asymptotically, $R_l(r)$ approach

$$R_l(r) \xrightarrow[r\to\infty]{} \frac{1}{ir}\left[(-i)^l e^{i(kr+\delta_l)} - i^l e^{-i(kr+\delta_l)}\right] \tag{2.12}$$

and therefore, $\psi(r)$ goes as

$$\psi \xrightarrow[r\to\infty]{} \frac{1}{2ikr}\sum_{l=0}^{\infty}(2l+1)P_l(\cos\theta)\left[(-1)^{l+1}e^{-ikr} + S_l e^{ikr}\right], \tag{2.13}$$

where $S_l = e^{2i\delta_l}$, at large r [34]. Next, we expand the plane wave e^{ikz} in Eq. (2.4), using Rayleigh's formula,

$$e^{ikz} \xrightarrow[r\to\infty]{} \frac{1}{2ikr}\sum_{l=0}^{\infty}(2l+1)P_l(\cos\theta)\left[(-1)^{l+1}e^{-ikr}+e^{ikr}\right] \tag{2.14}$$

and match the resulting expression to Eq. (2.13) [34]. This leads to the following formula for the scattering amplitude,

$$f(\theta) = \frac{1}{2ik}\sum_{l=0}^{\infty}(2l+1)(S_l-1)P_l(\cos\theta). \tag{2.15}$$

Substituting this expression in Eq. (2.8) and recalling the orthogonality relationship between the Legendre polynomials [34], the total-cross section is,

$$\sigma = \frac{4\pi}{k^2}\sum_{l=0}^{\infty}(2l+1)\sin^2\delta_l \tag{2.16}$$

In the following chapters, we will be considering ultracold collisions which are dominated the $l = 0$ or s-wave term. In this low-energy regime,

$$f_0 = \frac{1}{2ik}(e^{2i\delta_0}-1) \approx \frac{\delta_0}{k} \tag{2.17}$$

where δ_0 is the phase shift for the $l = 0$ partial wave, and σ is well-approximated by

$$\sigma \approx 4\pi a^2 \tag{2.18}$$

for distinguishable particles, or

$$\sigma \approx 8\pi a^2 \tag{2.19}$$

for identical particles, where $a = -\lim_{k\to 0}\frac{\delta_0}{k}$ is called the "scattering length" of the collision [34]. At higher energies, a is related to the s-wave phase shift by the effective range formula,

$$k\cot\delta_0 = -\frac{1}{a}+\frac{1}{2}r_e k^2 + ... \tag{2.20}$$

where r_e is the "effective range" of the potential well [17]. The scattering length fully encapsulates the properties of a low-energy collision. A negative a, such as in Figure 2-6, signifies that $V(r)$ fails to support a bound state near-zero energy; that is $\psi(r)$ fails to turn downward before the edge of the potential and therefore, cannot be matched a decaying exponential function which characterizes a bound state outside the well [17]. As the depth of the potential is increased, the wavelength of $\psi(r)$ decreases, "flattening out" the wavefunction beyond r_0, as depicted in Figure 2-7, and making a more negative until it eventually approaches $-\infty$ [17]. This means that $V(r)$ is on the verge of supporting a new bound state, and if its attractive well is made slightly deeper, the slope of $\psi(r)$ at r_0 will turn over so that a bound state is support and a is positive, as in Figure 2-8 [17].

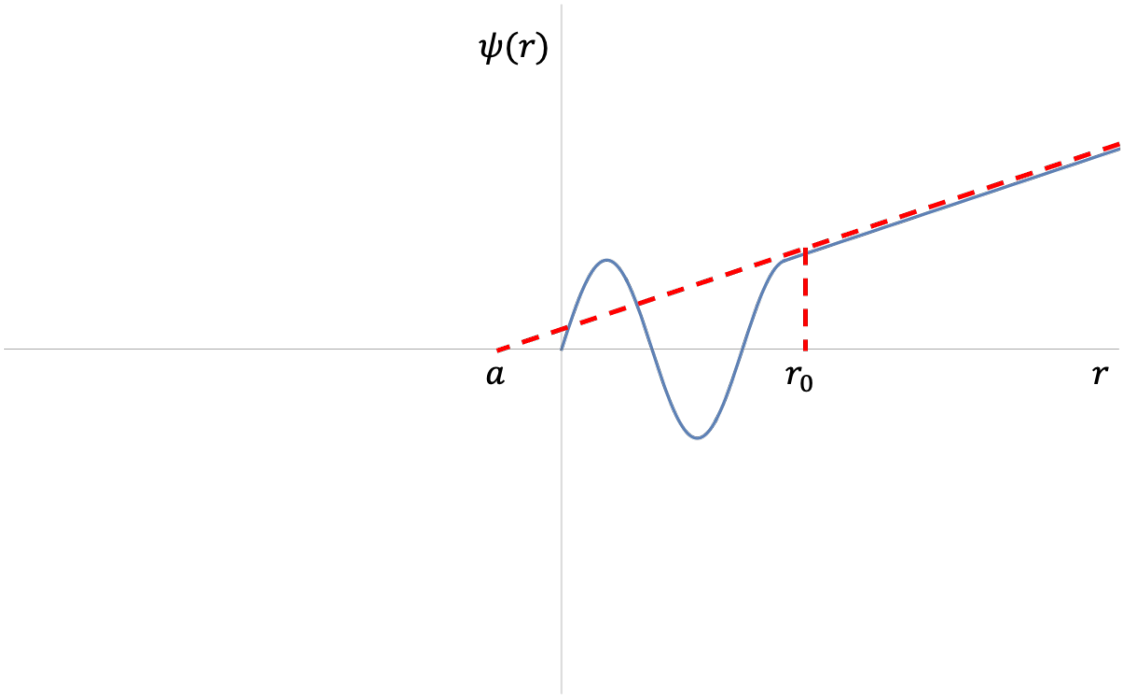

Figure 2-6: Scattering length a for a low-energy, two atom collision in an attractive, spherically symmetric potential of radius r_0. The scattering length is defined as the x-intercept of the wavefunction beyond r_0 and is negative here.

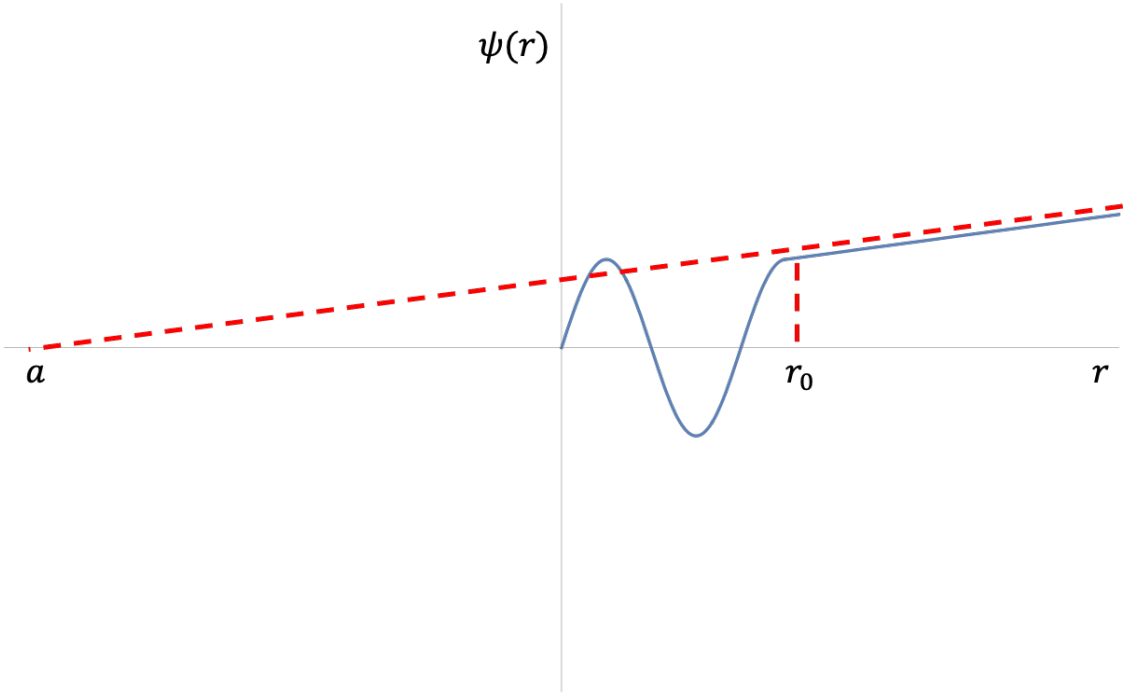

Figure 2-7: Scattering length a for a low-energy, two atom collision in a spherically symmetric potential of radius r_0 which is more attractive than that in Figure 2-6. Consequently, a is more negative and the wavefunction at large r has a more gradual slope.

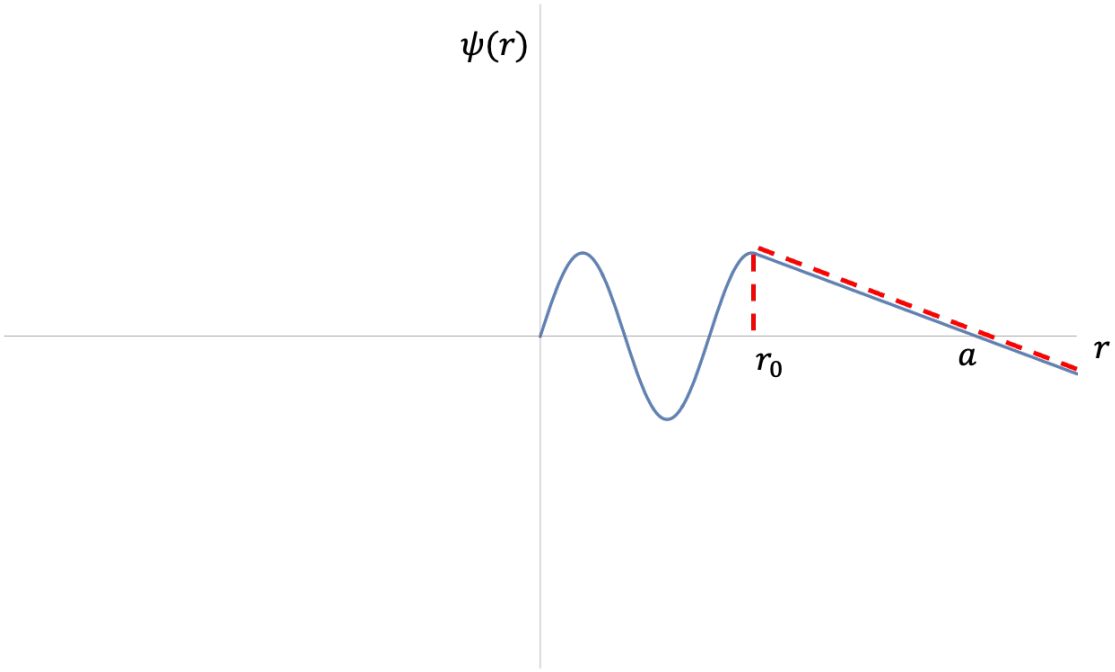

Figure 2-8: Scattering length a for a low-energy, two atom collision in a spherically symmetric potential of radius r_0 which is more attractive than that in Figure 2-7. The increase in the strength of the potential has decreased the wavelength of $\psi(r)$ at small r, causing $\psi(r)$ to turn downward at r_0, so that a bound state wavefunction can be match to it. As a result, a is now positive.

2.2 Multi-Channel Scattering Theory

The full relative wavefunction for an N-channel, two-body collision is,

$$\Psi(r,\xi) = \sum_{j=1}^{N} \psi_j(r)\Upsilon_j(\xi) \tag{2.21}$$

where the index j labels the N channels [18]. Here ψ_i are the respective channel wave functions, ξ represents all internal degrees of freedom, and $\Upsilon_i(\xi)$ are the eigenstates of the "internal Hamiltonian" (i.e., the Hamiltonian of the well-separated collision partners) H_ξ, with associated energy eigenvalues E_i. These E_i define the energy thresholds of the channels, while the internal states Υ_i correspond to the collision channels for the scattering process [18]. The full wavefunction satisfies,

$$\left[\frac{-\hbar}{2\mu}\frac{d^2}{dr^2} + H_\xi + W(r,\xi)\right]\Psi(r,\xi) = E\Psi(r,\xi), \tag{2.22}$$

where $W(r,\xi)$ is an operator that acts on functions of r and ξ and we assume that it vanishes as $r \to \infty$, and obeys the boundary condition,

$$\Psi(r,\xi) \xrightarrow[r\to\infty]{} \Upsilon_i(\xi)e^{ik_i z} + \sum_{j=1}^{N_o} f_{i\to j}(\theta)\frac{e^{ik_j r}}{r}\Upsilon_j(\xi) \tag{2.23}$$

Here N_o denotes the number of open channels and $k_i = \frac{\sqrt{2\mu(E-E_i)}}{\hbar}$ and $k_j = \frac{\sqrt{2\mu(E-E_j)}}{\hbar}$ are respective wavenumbers of the i^{th} and j^{th} channels.

Inserting the expansion for $\Psi(r,\xi)$ into Eq. (2.22) and taking the overlap with $\Upsilon_j(\xi)$, we arrive at the coupled-channels equation:

$$-\frac{\hbar}{2\mu}\nabla^2\psi_j(r) + \sum_j^N W_{ji}(r)\psi_i(r) = (E - E_j)\delta_{ji}\psi_j(r) \tag{2.24}$$

where $W_{ji}(r) = \int d\xi \Upsilon_j(\xi) W(r,\xi)\Upsilon_i(\xi)$ [18]. Similarly to the single-channel problem, the wavefunction $\psi_i(r)$ of an open channel should approach

$$\psi_j(r) \xrightarrow[r\to\infty]{} \propto e^{ik_i z}\delta_{ij} + f_{i\to j}(\theta)\frac{e^{ik_j r}}{r} \tag{2.25}$$

while that of a closed channel must go as

$$\psi_j(r) \xrightarrow[r\to\infty]{} \propto \frac{e^{-\kappa_j r}}{r} \tag{2.26}$$

with $\kappa_j = ik_j$ [18]. Like Eq. (2.4), the first term of Eq. (2.25) represents the incident wave in state Υ_i traveling the $\hat{z}$-direction, while the second term represents the scattered, spherical wave. Here, $f_{i\to j}$ is related to the probability that the particle will scatter out into the channel defined by Υ_j, and the effective cross section $d\sigma$ is given by,

$$d\sigma = \frac{k_j}{k_i}|f_{i\to j}|^2 d\Omega. \tag{2.27}$$

[18]. The total cross-section is given by

$$\sigma_{tot} = \sum \sigma_{i\to j} \tag{2.28}$$

where $\sigma_{i\to j}$ is the integral of Eq. (2.27) over all solid angles $d\Omega = r^2 \sin\theta d\theta$. For an elastic collision, the particles enter and exit in the same channel, and the total elastic cross section is,

$$\sigma_{el} = \sigma_{i\to i} = \int |f_{i\to i}|^2 d\Omega. \tag{2.29}$$

To determine $f_{i\to j}$, we follow a similar procedure as in Section 2.1. First, we expand the open channel wavefunction $\psi_i(r)$ as a superposition of partial waves,

$$\psi_i(r) = \sum_{l=0}^{\infty} \frac{u_l^i(r)}{r} P_l(\cos\theta), \tag{2.30}$$

substitute this expansion into Eq. (2.24), and take the overlap with $P_{l'}$:

$$-\frac{\hbar^2}{2\mu}\frac{\partial^2 u_l^i}{\partial r^2} + \frac{\hbar^2 l(l+1)}{2\mu r^2}u_l^i(r) + \sum_{j,l'} V_{l,l'}^{i,j}(r)u_{l'}^j(r) = (E - E_i)u_l^i(r) \tag{2.31}$$

[18]. Since we are assuming the interaction between the particles is spherically symmetric, $V^{i,j}_{l,l'}(r) = V_{ij}(r)\delta_{l,l'}$ and each partial wave can be treated separately [18]:

$$-\frac{\hbar^2}{2\mu}\frac{\partial^2 u^i_l}{\partial r^2} + \frac{\hbar^2 l(l+1)}{2\mu r^2}u^i_l(r) + \sum_j V^{i,j}_l(r)u^j_l(r) = (E - E_i)u^i_l(r). \tag{2.32}$$

Now, at large r, we assume that the elements of the potential matrix $V_{ij}(r)$ vanish and Eq. (2.32) becomes,

$$-\frac{\partial^2 u^i_l}{\partial r^2} + \frac{l(l+1)}{r^2}u^i_l(r) - k_i^2 u^i_l(r) = 0 \tag{2.33}$$

with $k_i^2 = \frac{2\mu(E-E_i)}{\hbar^2}$. The solutions to Eq. (2.33) depend on whether or not the i^{th} channel energetically accessible to the system. If the channel is closed, i.e., $E - E_i < 0$, then the solution is proportional to a decaying exponential

$$u^i_l \xrightarrow[r\to\infty]{} \propto e^{\kappa_i r}. \tag{2.34}$$

If the channel is open, i.e., $E - E_i > 0$, then the solution/wavefunction is a linear combination of the energy-normalized Riccati-Bessel functions $s_l(kr)$ and $c_l(kr)$ [42]:

$$u_{il,jl'}(r) \xrightarrow[r\to\infty]{} \delta_{i,j}\delta_{l,l'}s_l(k_i r) + K_{il,jl'}c_{l'}(k_j r) \tag{2.35}$$

where

$$s_l(k_i r) = k_i r j_l(k_i r) \xrightarrow[r\to\infty]{} \sqrt{\frac{2\mu}{\hbar^2\pi k_i}}\sin\left(k_i r - \frac{l\pi}{2}\right), \tag{2.36}$$

and

$$c_l(k_i r) = -k_i r n_l(k_i r) \xrightarrow[r\to\infty]{} \sqrt{\frac{2\mu}{\hbar^2\pi k_i}}\cos\left(k_i r - \frac{l\pi}{2}\right) \tag{2.37}$$

and $j_l(x)$ and $n_l(x)$ are the spherical Bessel functions of the first and second kind, respectively. Eq. (2.35) defines the "K-matrix", or "reaction matrix". The diagonal elements of these matrix are equal to the reaction amplitude $\tan\delta_l$ where δ_l is the phase shift [17]. In matrix form, Eq. (2.35) becomes,

$$U = s + Kc \tag{2.38}$$

where U is the solution matrix with elements $u_{il,jl'}(r)$ and s and c are diagonal matrices with elements $s_l(k_i r)\delta_{ij}\delta_{ll'}$ and $c_l(k_i r)\delta_{ij}\delta_{ll'}$, respectively. The asymptotic solution in the open channels can also be written in terms of incoming and outgoing waves,

$$\phi_{il,jl'} \xrightarrow[r\to\infty]{} \delta_{i,j}\delta_{l,l'}f^-_l(k_i r) - S_{il,jl'}f^+_{l'}(k_j r) \tag{2.39}$$

where

$$f^+_l(k_i r) = \sqrt{\frac{2\mu}{\hbar^2\pi k_i}}e^{i(k_i r - l\pi/2)} \tag{2.40}$$

and

$$f^-_l(k_i r) = \sqrt{\frac{2\mu}{\hbar^2\pi k_i}}e^{-i(k_i r - l\pi/2)} \tag{2.41}$$

[18]. Eq. (2.39) defines the "S-matrix", or "scattering matrix". The diagonal elements of these matrix are equal to the scattering amplitude $e^{2i\delta_l}$ [17]. In matrix form, Eq. (2.39) is,

$$\Phi = f^- - Sf^+. \tag{2.42}$$

Note, that s, c, f^-, f^+, K, S and U are $N_o \times N_o$ matrices. The S- and K-matrices are related by

$$S = (1 + iK)(1 - iK)^{-1} \tag{2.43}$$

[18]. After rewriting the asymptotic form of $\psi_i(r)$ in the terms of these matrices, we expand the plane wave $e^{ik_i z}$ using the Rayleigh formula as,

$$e^{ik_i z} = \sqrt{\frac{\hbar^2 \pi k_i}{2\mu}} \frac{1}{2k_i r} \sum_{l=0}^{\infty} i^{l-1}(2l+1)\big(f^+(k_i r) - f^-(k_i r)\big)P_l(\cos\theta) \tag{2.44}$$

so that Eq. (2.25) becomes,

$$\psi_j(r) = \delta_{ij}\left[\sqrt{\frac{\hbar^2 \pi k_i}{2\mu}} \frac{1}{2k_i r} \sum_{l=0}^{\infty} i^{l-1}(2l+1)\big(f^+(k_i r) - f^-(k_i r)\big)P_l(\cos\theta)\right] + f_{i\to j}(\theta)\frac{e^{ik_j r}}{r}. \tag{2.45}$$

Matching this expression to,

$$\psi_j(r) = \sum_{l=0}^{\infty} P_l(\cos\theta)\frac{\phi_{il,jl'}(r)}{r} \tag{2.46}$$

we find that $f_{i\to j}$

$$f_{i\to j} = \frac{1}{2i\sqrt{k_i k_j}} \sum_{l=0}^{\infty} (2l+1)(S_{il,jl'} - \delta_{ij}\delta_{ll'})P_l(\cos\theta). \tag{2.47}$$

For an s-wave collision this reduces to

$$f_{i\to i}^{l=0} = \sqrt{\frac{4\pi}{k_i k_j}} \frac{(S_{i,j} - \delta_{ij})}{2i}. \tag{2.48}$$

and the total elastic cross section for the $l = 0$ partial wave is,

$$\sigma_{el} = \sigma_{i\to i} = \frac{\pi}{k_i^2}|S_{i,i} - 1|^2. \tag{2.49}$$

In the succeeding chapters, our goal will be to accurately calculate this last quantity, σ_{el}, as a function of magnetic field B for multichannel s-wave collisions of alkali atoms. In doing so, we will be able to identify and predict the number, positions, and widths of Fano-Feshbach resonances, which appear as sharp features in the graphs of σ_{el} versus B, within these systems—parameters which are of interest to experimentalists. Moreover, for all of the calculations performed, we only consider elastic collision in which there is only one asymptotically open channel and typically four additional closed channels that contribute to the short-range physics.

Chapter 3

Properties of Ultracold Alkali Collisions

The first step in any scattering calculation is identifying the components of the interaction between the collision partners and the asymptotic dissociation channels of the collision. In this chapter, we will discuss the terms that comprise the total interaction potential $V(r)$ of two alkali atoms in their electronic ground states, beginning with the interactions of a single atoms which dominate $V(r)$ at very large r and define the collision channels. We then tackle the two-atom problem, outlining the full interaction potential, covering which quantum numbers are conserved in the collision, and discussing the various bases one could elect to work in.

3.1 Single Atom Interactions

Alkali atoms inhabit the leftmost column of the periodic table, including every element in group 1 except for hydrogen. In their ground state configuration, these atoms have a lone valence electron occupying a half-filled s-orbital. The stationary states of these atoms are characterized by their internal degrees of freedom, namely the spin $\vec{s}$ of the valence electron and the spin $\vec{i}$ of the atomic nucleus, and can be found by diagonalizing the Hamiltonian H,

$$H^{HZ} = H^{hf} + H^{Z} \tag{3.1}$$

where H^{hf} is the hyperfine interaction and H^{Z} is the Zeeman interaction.

3.1.1 Hyperfine Interaction

Within an atom, magnetic interactions couple the spin and angular momenta of the composite bodies of atom (i.e, the electrons and nucleus) to each other and to any externally applied magnetic field $\vec{B}$. The hyperfine interaction H^{hf} between the electronic and nuclear magnetic dipoles is one such perturbation, coupling the electronic spin $\vec{s}$ with the nuclear spin $\vec{i}$ into the total spin $\vec{f} = \vec{s} + \vec{i}$, ranging from $\left|\vec{s} + \vec{i}\right|$ to $\left|\vec{s} - \vec{i}\right|$ in integer steps. H^{hf} may be written as,

$$H^{hf} = \frac{A^{hf}}{2}(\vec{s} \cdot \vec{i}) \tag{3.2}$$

where A^{hf} is the hyperfine constant of the atomic species of interest in their electronic ground state. Table 3.1 lists the values of A^{hf} along with the nuclear spins for various alkali atoms and the electronic spin $\vec{s} = \frac{1}{2}$ for every alkali atom since each only has a single valence electron. Using the definition of $\vec{f}$, we can rewrite $(\vec{s} \cdot \vec{i})$ as $\frac{f^2 - s^2 - i^2}{2}$ and Eq. (3.2) as,

$$H^{hf} = \frac{A^{hf}}{2}\big(f^2 - s^2 - i^2\big). \tag{3.3}$$

The hyperfine effect splits the degeneracy in n, separating the electronic energy levels of the atom based on their value of f. Each of these "hyperfine levels" is $(2f+1)$-fold degenerate and characterized by the set of quantum numbers n, f, and the projection of f on the z-axis, m_f. That is, the set of states $|(s\ i)\ n\ f\ m_f\rangle$ are stationary states of H^{hf} with associated eigenvalues of $\frac{A^{hf}\hbar^2}{2}\big(f(f+1) - s(s+1) - i(i+1)\big)$. Note, however, that the projections of the electronic and nuclear spins along the z-axis, m_s and m_i, are not conserved by H^{hf} because this interaction "mixes" states with different m_s and m_i together. In other words, the states $|(s\ i)\ n\ f\ m_f\rangle$ are linear combinations of the states $|n\ s\ m_s\ i\ m_i\rangle$,

$$|(s\ i)\ n\ f\ m_f\rangle = \sum_{m_s, m_i} C^{f,m_f}_{m_s,m_i}\, |n\ s\ m_s\ i\ m_i\rangle \tag{3.4}$$

where $C^{f,m_f}_{m_s,m_i}$ are the appropriate Clebsch-Gordan coefficients.

3.1.2 Zeeman Interaction

When an atom is placed in a uniform external field $\vec{B}$, the electronic energy levels shift and split due to the coupling of $\vec{B}$ with the nuclear and electronic magnetic moments. This phenomenon is known as the Zeeman effect, and for an alkali atom in its ground state (with $l = 0$), the perturbation caused by this interaction is given by,

$$H^Z = -(\vec{\mu_s} + \vec{\mu_i}) \cdot \vec{B} \tag{3.5}$$

where $\vec{\mu_s}$ and $\vec{\mu_i}$ are the magnetic dipole moments of the valence electron and nucleus, respectively. $\vec{\mu_s}$ and $\vec{\mu_i}$ can be expressed as $\vec{\mu_s} = -g_s \mu_B \vec{s}$ and $\vec{\mu_i} = -g_i \mu_B \vec{i}$ where $\mu_B = \frac{e\hbar}{2m_e} = 1.3996244936142$ MHz/Gauss is the Bohr magneton, $g_s = 2.00231930436256$ is the electronic gyromagnetic ratio expressed in units of μ_B, g_i is the nuclear gyromagnetic ratio expressed in units of μ_B, $\vec{s}$ is the electronic spin and $\vec{i}$ is the nuclear spin. The value for g_i for each alkali species can be found in Table 3.1. Choosing $\vec{B}$ to lie along the z-axis and substituting in the expressions for $\vec{\mu_s}$ and $\vec{\mu_i}$, H^Z becomes,

$$H^Z = \mu_B B(g_s s_z + g_i i_z) \tag{3.6}$$

where B is the magnitude of the applied field and s_z and i_z are operators which pick out the component of the electronic and nuclear spins along the $\hat{z}$-axis. As the magnitude of the applied field B increases, the Zeeman effect begins to dominate the hyperfine interaction, breaking the degeneracy in f and causing the hyperfine energy levels to shift and separate further. Good quantum numbers for the Zeeman interaction are n, i, s, m_s, and m_i and eigenstates of H^Z are $|n\ s\ m_s\ i\ m_i\rangle$ with corresponding eigenvalues $\mu_B B\hbar(g_s m_s + g_i m_i)$. The total angular momentum f and its z-projection m_f are no longer good quantum

numbers because the stationary states of Eq. (3.6) are linear combinations of states with different values of theses quantities. Put another way, the operators H^Z and H^{HF} are not diagonal in the same basis because the operators s_z and i_z do not commute with f^2 and therefore, one cannot find states that are simultaneous eigenstates of both H^Z and H^{hf}.

Moreover, as a result of this fact, there is some freedom in deciding which atomic basis to work in. Presently, we have elected to use the single-atom hyperfine basis defined as $|(s\ i)\ n\ f\ m_f\rangle$, since at zero field, these are the eigenstates of Eq. (3.1). Another choice is the Zeeman basis with states $|n\ s\ m_s\ i\ m_i\rangle$; however, the Hamiltonian is only diagonal in this basis as $B \to \infty$ and therefore, it is less advantageous to construct H in terms of the $|n\ s\ m_s\ i\ m_i\rangle$ kets. Figures 3-1 and 3-2 show the hyperfine and Zeeman splitting of the atomic ground state of ^{6}Li and ^{7}Li.

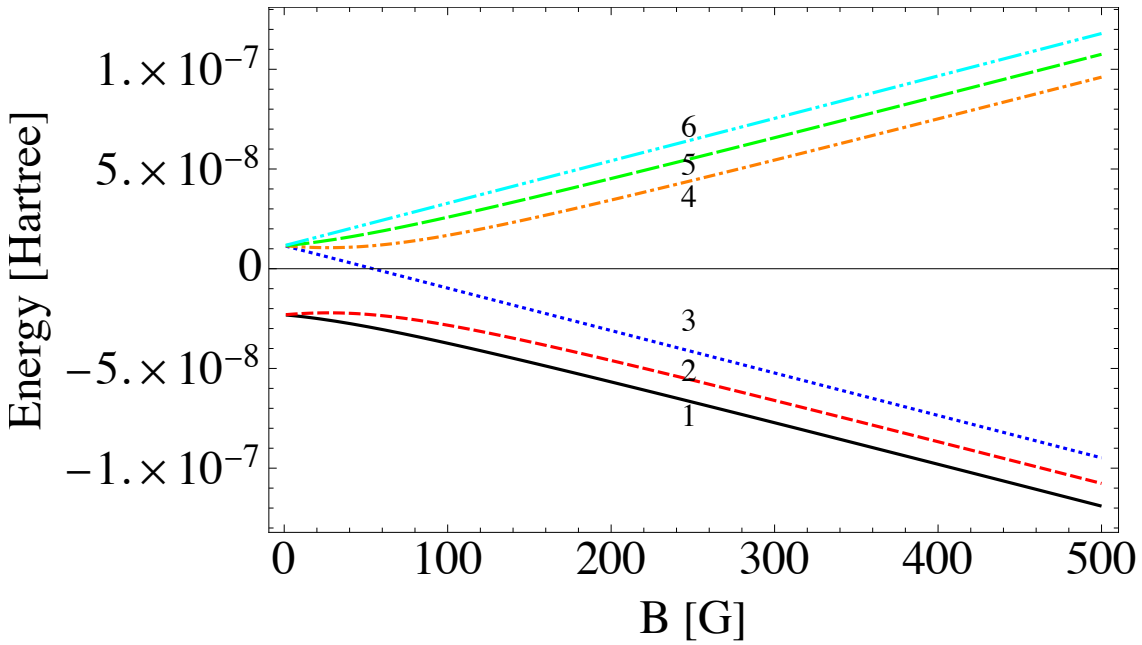

Figure 3-1: Hyperfine and Zeeman splitting of ^{6}Li plotted versus magnetic field B. The labels correspond following hyperfine states at zero field: $1 = \left|\frac{1}{2}\ \frac{1}{2}\right\rangle$, $2 = \left|\frac{1}{2}\ -\frac{1}{2}\right\rangle$, $3 = \left|\frac{3}{2}\ -\frac{3}{2}\right\rangle$, $4 = \left|\frac{3}{2}\ -\frac{1}{2}\right\rangle$, $5 = \left|\frac{3}{2}\ \frac{1}{2}\right\rangle$, $6 = \left|\frac{3}{2}\ \frac{3}{2}\right\rangle$.

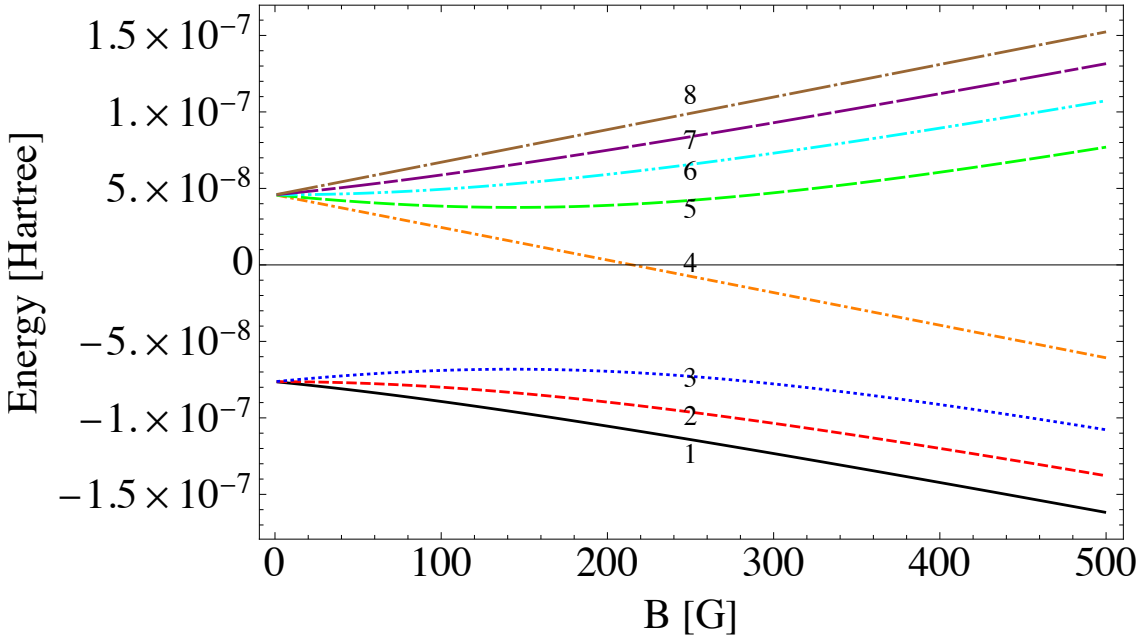

Figure 3-2: Hyperfine and Zeeman splitting of ^{7}Li plotted versus magnetic field B. The labels correspond following hyperfine states at zero field: $1 = |1\ 1\rangle$, $2 = |1\ 0\rangle$, $3 = |1\ -1\rangle$, $4 = |2\ -2\rangle$, $5 = |2\ -1\rangle$, $6 = |2\ 0\rangle$, $7 = |2\ 1\rangle$, $8 = |2\ 2\rangle$.

Isotope	A^{hf} (MHz)	g_i	$\vec{i}$	mass (amu)
^{6}Li	152.1368407(20)	-0.0004476540(3)	1	6.0151223
^{7}Li	401.7520433(5)	-0.001182213(6)	3/2	7.016004
^{23}Na	885.8130644(5)	-0.0008046108(8)	3/2	22.98976928
^{39}K	230.8598601(3)	-0.00014193489(12)	3/2	38.963708
^{40}K	-285.7308(24)	0.000176490(34)	4	39.964008
^{85}Rb	1011.910813(2)	-0.0002936400(6)	5/2	84.911789738
^{87}Rb	3417.34130642(15)	-0.0009951414(10)	3/2	86.909180527

Table 3.1: Hyperfine constants A^{hf}, nuclear g-factors g_i, nuclear spins $\vec{i}$, and masses for various isotopes of alkali atoms. The values for the A^{hf}'s and g_i's come from [2].

3.2 Two Atom Interactions

The full interaction potential for two ground state alkali atoms can be broken down into three components: (1) the Born-Oppenheimer potentials which correspond to the ground singlet $X^1\Sigma_g^+$ ($S = 0$) and lowest-lying triplet $a^3\Sigma_u^+$ ($S = 1$) molecular states, (2) the hyperfine interaction of each atom H_α^{HF} and (3) Zeeman interactions H_α^Z of each atom:

$$P_0 V_0(r) + P_1 V_1(r) + \sum_{\alpha=1}^{2} \left(H_\alpha^{hf} + H_\alpha^Z\right). \tag{3.7}$$

Here $P_{0/1}$ are the singlet and triplet projection operators, $V_{0/1}(r)$ are the ground state singlet and triplet Born-Oppenheimer potentials, and the Greek letter α indexes the atoms. The projection operators are given by

$$P_S = \sum_{I M_S M_I} |S\ M_S\ I\ M_I\rangle \langle S\ M_S\ I\ M_I| \tag{3.8}$$

where S is the total electric spin quantum number ranging from $|\vec{s_1} - \vec{s_2}|$ to $|\vec{s_1} + \vec{s_2}|$ in integer steps, M_S the total electronic spin projection range from $-S$ to S in integer steps, I is total nuclear spin quantum number ranging from $\left|\vec{i_1} - \vec{i_2}\right|$ to $\left|\vec{i_1} + \vec{i_2}\right|$ in integer steps, and M_I is the total nuclear spin projection ranging from $-I$ to I in integer steps. Eq. (3.8) picks out the portion of the two-atom state $|\alpha\beta\rangle$ along the singlet $|0\ M_S\ I\ M_I\rangle$ or triplet $|1\ M_S\ I\ M_I\rangle$ molecular state. The Born-Oppenheimer potentials describe the interaction between the atoms. Refs.[45] and [44] provide analytical forms for the $X^1\Sigma_g^+$ and $a^3\Sigma_u^+$ potentials of $^6Li_2$ and $^7Li_2$, ref.[31] for $^6Li_2$, ref.[14] for $^{39}K_2$ and $^{40}K_2$, and ref.[52] for $^{87}Rb_2$ and $^{85}Rb_2$.

It is important to note that all of the operators—$H_\alpha^{hf}, H_\alpha^Z$, and $P_{0/1}$—in Eq. (3.7) cannot be diagonalized in the same basis. Recall from the previous section that the hyperfine and Zeeman operators (for each atom) do not commute, and therefore do not share the same eigenstates. Likewise, the singlet and triplet projection operators, $P_{0/1}$ are not diagonal in the stationary states of the hyperfine interaction because the total spin operator $\vec{S} = \vec{s_1} + \vec{s_2}$ does not commute with total angular momentum operator f^2 for each atom. However, $P_{0/1}$ and H_α^Z do commute with each other. Thus, the total Hamiltonian will have off-diagonal elements no matter which basis we choose to construct Eq. (3.7) in. It is exactly this off-diagonal nature of the Hamiltonian which necessitates a full "coupled-channels" calculation where each collisional channel is labeled by the internal states of the individual atoms. However, this does not mean that all channels will couple together. Because the potential described by Eq. (3.7) is central (any dipolar interaction between the atoms has been neglected) the total angular momentum of the system cannot change during the interaction and the total spin projection $M_F = m_{f_1} + m_{f_2} = M_S + M_I$ must be conserved. This means that states with the same M_F will couple together.

Moreover, since each term in Eq. (3.7) is characterized by a different set of "good" quantum numbers, there is some freedom in choosing which basis set to use for solving a scattering problem. One could select to work in the "molecular basis" given by

$$|\alpha\beta\rangle = |(s_1\ s_2)\ S\ M_S\ (i_1\ i_2)\ I\ M_I\rangle \tag{3.9}$$

where the electronic and nuclear spins of the composite atoms are coupled, resulting in the total electronic spin $\vec{S} = \vec{s_1} + \vec{s_2}$ and the total nuclear spin $\vec{I} = \vec{i_1} + \vec{i_2}$ and M_S and M_I are their respective projections. The projection operators $P_{0/1}$ and the combined Zeeman interactions of the particles $H_1^Z + H_2^Z$ are diagonal in this basis. However, as noted above the hyperfine interaction for each atom is proportional the term $\vec{s} \cdot \vec{i}$, which couples its electronic and nuclear spin to some total angular momentum $\vec{f}$, the magnitude of which ranges from $|s - i|$ to $|s + i|$ in integer steps. This means that the f, s, and i values for each atom are good quantum numbers for describing H_α^{HF} and it will, therefore, not be diagonal in the molecular basis.

Another choice is the "uncoupled-atomic basis":

$$|\alpha\beta\rangle = |s_1\ m_{s_1}\ i_1\ m_{i_1}\ s_2\ m_{s_2}\ i_2\ m_{i_2}\rangle\,. \tag{3.10}$$

Like the molecular basis, both the projection operators and Zeeman interactions are diagonal in this basis, but the hyperfine interactions of the individual atoms are not. Finally, one could also elect to use "two-atom hyperfine basis" with states

$$|\alpha\beta\rangle = |(s_1\ i_1)\ f_1\ m_{f_1}\ (s_2\ i_2)\ f_2\ m_{f_2}\rangle\,. \tag{3.11}$$

Only the hyperfine interaction is diagonal in this basis, $P_{0/1}$ and H_α^Z are not.

One also must take into account whether the collision partners are identical when selecting which basis set to use. Following the notation of refs. [51] and [37] we can properly represent the symmetry requirements for identical bosons or fermions by defining the basis kets as,

$$|\{\alpha\beta\}\rangle = \frac{|\alpha\beta\rangle \pm (-1)^l\,|\beta\alpha\rangle}{\sqrt{2(1+\delta_{\alpha,\beta})}}. \tag{3.12}$$

where the Greek letters refer to the internal states of the individual atoms, the $\pm$ specifies if the particles are bosons or fermions and the factor $(-1)^l$ accounts for the dependence of the internal/spin state on the symmetry of the spatial part of the wavefunction. For our collisions of two alkali atoms, we have chosen to work in a symmetrized version of the atomic hyperfine basis given by,

$$|\{f_1\ m_{f_1}\ f_2\ m_{f_2}\}\rangle = \frac{|f_1\ m_{f_1}\ f_2\ m_{f_2}\rangle \pm (-1)^l\,|f_2\ m_{f_2}\ f_1\ m_{f_1}\rangle}{\sqrt{2(1+\delta_{1,2})}}. \tag{3.13}$$

We have elected to use this basis because the states $|\{f_1\ m_{f_1}\ f_2\ m_{f_2}\}\rangle$ are the eigenstates of the threshold Hamiltonian,

$$H^{thresh} = \sum_{\alpha=1}^{2} H_\alpha^{hf} + H_\alpha^Z \tag{3.14}$$

in the limit that $B = 0$, and therefore, define the collision channels at zero field and their corresponding eigenvalues define the channel thresholds. In Section 3.6, we give expressions for the elements of the projection operators and the total two-atom hyperfine/Zeeman operator in the symmetrized hyperfine basis.

At finite B, the collision channels and energy thresholds are the eigenstates and eigenvalues, respectively, of H^{thresh}. Figures 3-3 and 3-4 show the energy thresholds for collisions of $^6Li_2$ with $M_F = 0$ and $^7Li_2$ with $M_F = 2$.

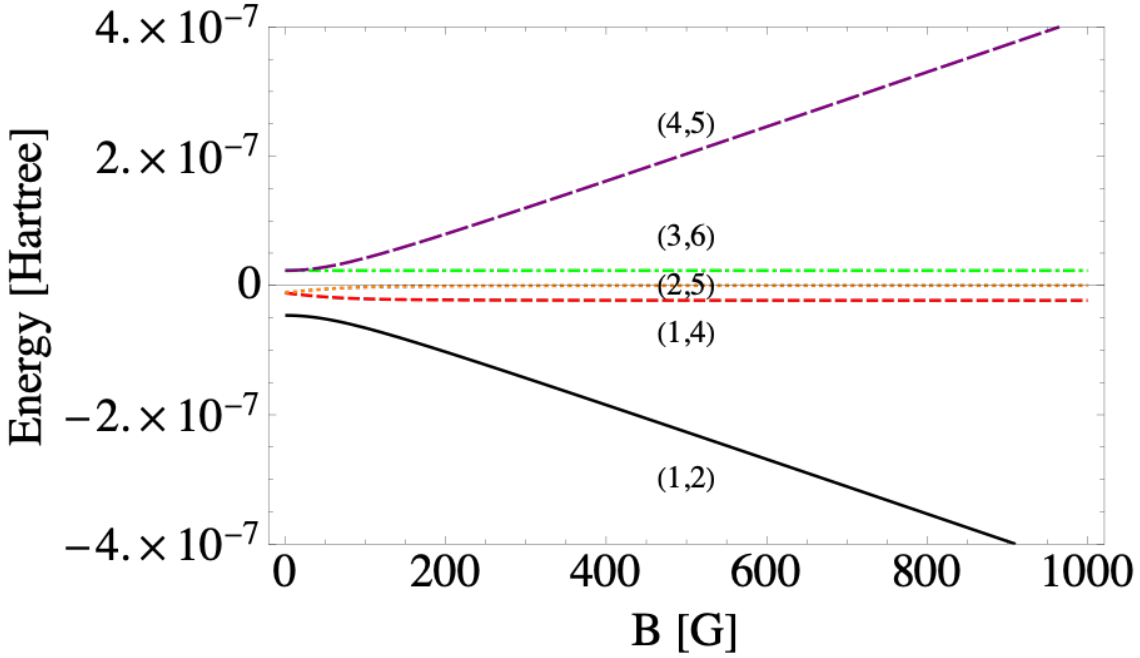

Figure 3-3: Hyperfine and Zeeman splitting for $^6Li_2$ with $M_F = 0$. Each threshold is labeled by the states of the individual atoms seen in Figure 3-1.

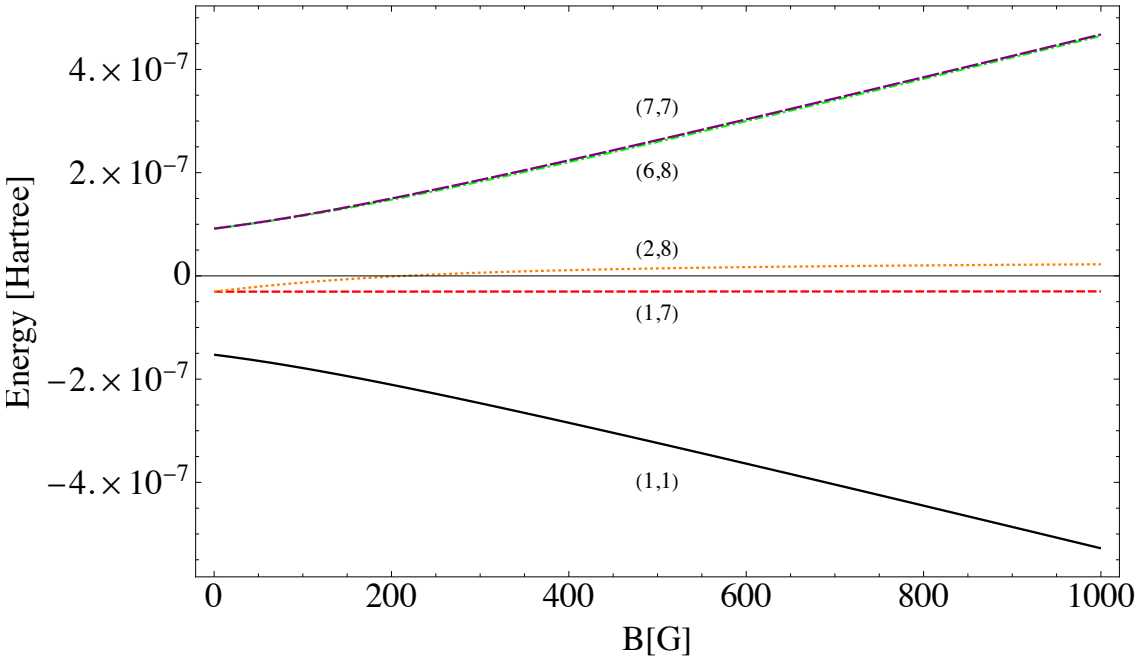

Figure 3-4: Hyperfine and Zeeman splitting for $^7Li_2$ with $M_F = 2$. Each threshold is labeled by the states of the individual atoms seen in Figure 3-2.

3.3 Operators in Symmetrized Hyperfine Basis

3.3.1 Hyperfine and Zeeman Interactions

The matrix elements of the two-atom hyperfine/Zeeman Hamiltonian $H_1^{HZ} + H_2^{HZ}$ in the symmetrized hyperfine basis $|\{\alpha\beta\}\rangle = |\{f_1\ m_{f_1}\ f_2\ m_{f_2}\}\rangle$ are,

$$\begin{aligned}\left\langle\{\alpha'\beta'\}\right| H_1^{HZ} + H_2^{HZ} \left|\{\alpha\beta\}\right\rangle = \frac{1}{\sqrt{(1+\delta_{\alpha'\beta'})(1+\delta_{\alpha\beta})}}\Big[\left\langle\alpha'\right| H^{HZ} \left|\alpha\right\rangle \delta_{\beta\beta'} \\ + \left\langle\beta'\right| H^{HZ} \left|\beta\right\rangle \delta_{\alpha\alpha'} \pm (-1)^l \big(\left\langle\alpha'\right| H^{HZ} \left|\beta\right\rangle \delta_{\beta'\alpha} + \left\langle\beta'\right| H^{HZ} \left|\alpha\right\rangle \delta_{\beta\alpha'} \big) \Big]\end{aligned} \tag{3.15}$$

where the terms $\langle\alpha'| H^{HZ} |\alpha\rangle$ are the elements of the $H_\alpha^{HZ} = H_\alpha^{hf} + H_\alpha^Z$ operator in the single atom hyperfine basis $|\alpha\rangle = |f m_f\rangle$:

$$\begin{aligned}\left\langle f'\ m'_f\right| H^{HZ} \left|f\ m_f\right\rangle = \frac{A^{hf}}{2}\big[f(f+1) - s(s+1) - i(i+1)\big]\delta_{ff'}\delta_{m_f m'_f} \\ +\mu_B B\sqrt{(2f'+1)(2f+1)} \sum_{m_s m_i} (g_s m_s + g_i m_i) \begin{pmatrix} s & i & f' \\ m_s & m_i & -m'_f \end{pmatrix} \begin{pmatrix} s & i & f \\ m_s & m_i & -m_f \end{pmatrix} \delta_{m_f m'_f}\end{aligned} \tag{3.16}$$

[37].

3.3.2 Projection Operators

In the symmetrized hyperfine basis, the elements of the singlet and triplet projection operators $P_{0/1}$ become,

$$\begin{aligned}\left\langle\{f'_1\ m'_{f_1}\ f'_2\ m'_{f_2}\}\right| P_{0/1} \left|\{f_1\ m_{f_1}\ f_2\ m_{f_2}\}\right\rangle = \\ \frac{\left\langle f'_1\ m'_{f_1}\ f'_2\ m'_{f_2}\right| P_{0/1} \left|f_1\ m_{f_1}\ f_2\ m_{f_2}\right\rangle \pm (-1)^l \left\langle f'_2\ m'_{f_2}\ f'_1\ m'_{f_1}\right| P_{0/1} \left|f_2\ m_{f_2}\ f_1\ m_{f_1}\right\rangle}{\sqrt{2(1+\delta_{12})}}\end{aligned} \tag{3.17}$$

[37]. Here $\left\langle f'_1\ m'_{f_1}\ f'_2\ m'_{f_2}\right| P_{0/1} \left|f_1\ m_{f_1}\ f_2\ m_{f_2}\right\rangle$ are the elements of $P_{0/1}$ in the unsymmetrized hyperfine basis $|f_1\ m_{f_1}\ f_2\ m_{f_2}\rangle$,

$$\begin{aligned}\left\langle f'_1\ m'_{f_1}\ f'_2\ m'_{f_2}\right| P_{0/1} \left|f_1\ m_{f_1}\ f_2\ m_{f_2}\right\rangle = \sum_{S\ I\ m_S\ m_I} \delta_{S,(1\ or\ 0)} \left\langle S\ m_S\ I\ m_I | f_1\ m_{f_1}\ f_2\ m_{f_2}\right\rangle \times \\ \left\langle S\ m_S\ I\ m_I \right| f'_1\ m'_{f_1}\ f'_2\ m'_{f_2}\big\rangle .\end{aligned} \tag{3.18}$$

Eq. (3.18) is used for collisions between distinguishable atoms and is found by expanding the hyperfine states into the basis functions which are eigenvalues of the triplet and singlet operators:

$$\left|f_1\ m_{f_1}\ f_2\ m_{f_2}\right\rangle = \sum_{S\ I\ m_S\ m_I} \left|S\ m_S\ I\ m_I\right\rangle \left\langle S\ m_S\ I\ m_I | f_1\ m_{f_1}\ f_2\ m_{f_2}\right\rangle \tag{3.19}$$

where $|S\ m_S\ I\ m_I\rangle\,\langle S\ m_S\ I\ m_I|f_1\ m_{f_1}\ f_2\ m_{f_2}\rangle$ are the appropriate Clebsch-Gordan coefficient given by [37],

$$\begin{aligned}\langle S\ m_S\ I\ m_I|f_1\ m_{f_1}\ f_2\ m_{f_2}\rangle = \\ (-1)^{2i_2-2s_1-m_{f_1}-m_{f_2}-m_S-m_I}\sqrt{(2f_1+1)(2f_2+1)(2S+1)(2I+1)}\times \\ \sum_{m_{s_1}m_{i_1}m_{s_2}m_{i_2}}\begin{pmatrix} s_1 & i_1 & f_1 \\ m_{s_1} & m_{i_1} & -m_{f_1}\end{pmatrix}\begin{pmatrix} s_2 & i_2 & f_2 \\ m_{s_2} & m_{i_2} & -m_{f_2}\end{pmatrix}\times \\ \begin{pmatrix} s_1 & s_2 & S \\ m_{s_1} & m_{s_2} & -m_S\end{pmatrix}\begin{pmatrix} i_1 & i_2 & I \\ m_{i_1} & m_{i_2} & -m_I\end{pmatrix}\end{aligned} \tag{3.20}$$

Chapter 4

Quantum Defect Theory

4.1 History of Quantum Defect Theory

The concept of the quantum defect arose from modifications made to the Bohr-Sommerfeld model of the hydrogen atom to account for the effects that interactions between electrons had on the spectra of non-hydrogenic atoms (i.e., atoms containing more than one electron). In the early 1910's, Niels Bohr and Arnold Sommerfeld had built a semi-classical model that accurately described hydrogen atom, including its fine structure, and ions containing a single electron [33]. However, the Bohr-Sommerfeld model had been specifically tailored to hydrogenic particles–it did not account for interactions between electrons–and failed to accurately reproduce the spectral lines of more complicated atoms [4] [5] [50]. In 1921, Erwin Schrodinger attempted to generalize the Born-Sommerfeld model to include these effects, introducing what he called the "Quantendefekt," or quantum defect in English, and the idea of an effective quantum number [48]. Expanding on the Bohr-Sommerfield model, Schrodinger considered the path or motion of a valence, or outermost, electron around the atomic nucleus, dividing it into two different regions based on the distance separating the two bodies [48]. Schrodinger's justification for this division that was at long-range, the valence electron was almost entirely shielded from the nucleus by the other electrons, and therefore, it only "saw" an effective nuclear charge $Z = 1$, while at short-range, the electron would feel the full nuclear charge Z [48].

Schrodinger's concept of the quantum defect remained in his later quantum theory of wave mechanics [49], which, along with Heisenberg's matrix formulation [25], forms the basis of modern quantum theory. In modern quantum theory, the quantum defect, now denoted as μ, is related to the short-range phase shift $\delta_{sr} = \mu\pi$ that an electron accumulates when it penetrates the atomic core, in addition to the phase shift from the effective Coulomb potential that it experiences when it is farther from the nucleus [46]. Moreover, the key idea behind Schrodinger's "Quantendefekt"—i.e., the separation of the electronic interaction into short- and long-range regions—became the basis for modern quantum defect theory (QDT).

Over the decades, this idea has been used to compute bound to bound state transitions of atoms [3], explore photoionization [7], and to develop a multichannel quantum defect theory (MQDT) to analyze complex atomic [19] and molecular [15] [16] spectra. In the 1980's, MQDT was further generalized to work

for other long-range potentials besides the the typical Coulomb interaction [21] [22] [39] [43]. Recently, it has been applied to atomic and molecular collisions [29], especially cold or ultracold collisions [9] [40] [11] to predict scattering observables like the locations and width of Fano-Feshbach resonances.

4.2 Application of QDT to Ultracold Collisions

Collisions between ultracold atoms are exceedingly complex. Atoms contain a multitude of internal states defined by their nuclear and electronic spins as we saw in Chapter 3. What's more, all of these states have to be accounted for since their associated energies are typically large compared to the kinetic energy of the atoms. This means that one has to simultaneously solve a set of coupled radial Schrodinger equations, leading to expensive, intensive computations.

This is where MQDT comes in. Because it takes advantage of the natural separation of the energy and length scales in collision problems, MQDT greatly reduces the computation time and complexity. In much the same fashion as Schrodinger, modern QDT separates the collision problem into short-range and long-range regions. At small internuclear separation distances r, the interaction between the atoms is characterized by the potentials wells of the ground state singlet and lowest lying triplet Born-Oppenheimer potentials, $V_0(r)$ and $V_1(r)$. The depths of these wells, at $10^{-2} - 10^{-4}$ Hartree, are much greater than the range of ultra-low collision energies $E^{collision}$ that we are interested in. This means that the wavefunction in this region and the short-range phase shifts (and thus, the quantum defects) are largely insensitive to variations in the collision energy and any applied electric or magnetic fields. This means that one only needs to perform this short-range calculation at a single value of energy and field. Beyond about 30 a_0, the strong attractive pull of these potential wells is negligible and the interatomic interaction, instead, is characterized by a sum of attractive van der Waals terms with energies on the order of 10^3 Hartree. For alkali atoms, this sum is given by

$$V_{LR}(r) = -\frac{C_6}{r^6} - \frac{C_8}{r^8} - \frac{C_{10}}{r^{10}} \tag{4.1}$$

where C_6, C_8, and C_{10} are the appropriate dispersion coefficients [35]. Because V_{LR} is weaker than the strong potential wells which dominate at short-range, the physics of this region displays greater sensitivity to $E^{collision}$ and any external fields. Eq. (4.1) quickly vanishes as $r \to \infty$, and out at these separation distances, the colliding particles are essentially non-interacting and the system is defined by the individual internal states of the atoms. After separating the atomic collision into these three regions, the solutions to the Schrodinger equation in each are stitched together by applying appropriate boundary conditions (i.e., requiring that the wavefunction and its derivative are continuous) where the regions overlap with each other. These boundary conditions lead to expressions for the quantum defects and the so-called "QDT" parameters.

In sum, MQDT describes both the long-range physics and short-range physics in terms of a collection of simple parameters. The long-range parameter are analytical functions of energy which can be well-approximated by simple expressions in the limit of small collision energy, while the short-range parameters are nearly independent of energy and field. The accuracy of this procedure relies on the availability of a pair

of accurate, linearly independent reference wave functions in each channel at large r. The standardization technique of Ruzic *et al.* ensures the maximal linear independence between reference functions even for higher partial wave angular momentum [46] .

We will begin our discussion of quantum defect theory by first considering a single-channel collision of two ^{7}Li atoms, calculating the background scattering length and bound states of one channel, then generalizing the theory for N collision channels, we will see how QDT can be used to predict the number, positions, and widths of Fano-Feshbach resonances in ultracold alkali collisions.

The total interaction for the $^7Li_2$ s-wave collision, with a total orbital angular momentum $\vec{L}_{tot} = \vec{l_1}+\vec{l_2}+\vec{L} = 0$ where l_1 and l_2 are the orbital angular momenta of the separated atoms and L is the relative orbital angular momentum of the two collision partners, is given by,

$$V(r) = P_0 V_0(r) + P_1 V_1(r) + \sum_{\alpha=1}^{2} H_\alpha^{HZ} \tag{4.2}$$

where the index α labels the two atoms, H^{HZ} is the hyperfine/Zeeman interaction for each atom which is given by Eq. (3.1), $P_{0/1}$ are the singlet and triplet projection operators and $V_0(r)$ and $V_1(r)$ are the Born-Oppenheimer potentials which correspond to the ground state singlet and lowest lying triplet molecular states, respectively. The behavior of the Born-Oppenheimer potentials, $V_0(r)$ and $V_1(r)$, for $^7Li_2$ is shown in Figure 4-1. At long-range, $V_0(r)$ and $V_1(r)$ both approach Eq. (4.1), while at small r, they are characterized by deep wells. Moreover, because the $-\frac{C_6}{r^6}$ term dominates V_{LR}, it is advantageous to cast Eq. (4.2) in terms of the van der Waals length $\beta = \left(\frac{2\mu C_6}{\hbar^2}\right)^{1/4}$ and energy $E_\beta = \frac{\hbar^2}{2\mu\beta^2}$, where μ is the reduced mass of the system and C_6 is the appropriate dispersion coefficient. For $^7Li_2$, $\beta = 65.2049\ a_0$, $E_\beta = 1.8390 \times 10^{-8}$ Hartree, $\mu = 6394.7$ a.u., and $C_6 = 1393.39$ Hartree/a_0^6.

We initially construct $V(r)$ in the symmetrized hyperfine basis using Eqs.(3.15) and (3.17) to calculate the matrix elements of P_0, P_1 and H_α^{HZ}. Recall that because $V(r)$ is central, the z-projection of the total spin M_F is conserved and thus we need only to consider the symmetrized hyperfine states with $m_{f_\alpha}+m_{f_\beta} = M_F$ when calculating the elements of these operators. For our present calculations we will consider an $^7Li_2$ collision with $M_F = 2$. The $^7Li_2$ states $\left|\{f_\alpha\ m_{f_\alpha}\ f_\beta\ m_{f_\beta}\}\right\rangle$ with $M_F = 2$ are:

$$\begin{aligned}
&|\{1\ 1\ 1\ 1\}\rangle \\
&|\{1\ 1\ 2\ 1\}\rangle \\
&|\{1\ 0\ 2\ 2\}\rangle \\
&|\{2\ 0\ 2\ 2\}\rangle \\
&|\{2\ 1\ 2\ 1\}\rangle\,.
\end{aligned} \tag{4.3}$$

It should be noted that the states in Eq. (4.3) only correspond to the interaction channels at zero-field; in general, the channels are the eigenstates of,

$$H^{HZ} = H_1^{HZ} + H_2^{HZ} \tag{4.4}$$

and the channel thresholds E_i^{thresh} are eigenvalues of Eq. (4.4), which can be seen in Figure 3-4 as functions of magnetic field B.

4.3 Single Channel QDT

For our single-channel collision, we will calculate the bound states of the lowest lying $^7Li_2$ channel with $M_T = 2$. This channel corresponds to the symmetrized hyperfine state $|\{1\ 1\ 1\ 1\}\rangle$ state at $B = 0$ and the curve labeled (1, 1) in Figure 3-4 shows its energy threshold as a function of magnetic field. The total Hamiltonian in van der Waals units is,

$$H = \frac{d^2}{dr^2} + V(r) + H^{HZ} \tag{4.5}$$

where $V(r) = P_0 V_0(r) + P_1 V_1(r)$ and $H^{HZ} = H_\alpha^{HZ} + H_\beta^{HZ}$. Here, P_0, P_1, and H_α^{HZ} are just single elements,

$$P_0 = \langle\{1\ 1\ 1\ 1\}|\, P_0\, |\{1\ 1\ 1\ 1\}\rangle\,, \tag{4.6}$$

$$P_1 = \langle\{1\ 1\ 1\ 1\}|\, P_1\, |\{1\ 1\ 1\ 1\}\rangle\,, \tag{4.7}$$

and

$$H^{HZ} = \langle\{1\ 1\ 1\ 1\}|\, H_\alpha^{HZ} + H_\beta^{HZ}\, |\{1\ 1\ 1\ 1\}\rangle\,, \tag{4.8}$$

rather than matrices, and are evaluated using Eqs.(3.15) and (3.17). P_0 and P_1 pick out the portion of $|\{1\ 1\ 1\ 1\}\rangle$ along the singlet and triplet states, respectively, and H^{HZ} is equal to the channel threshold at zero field.

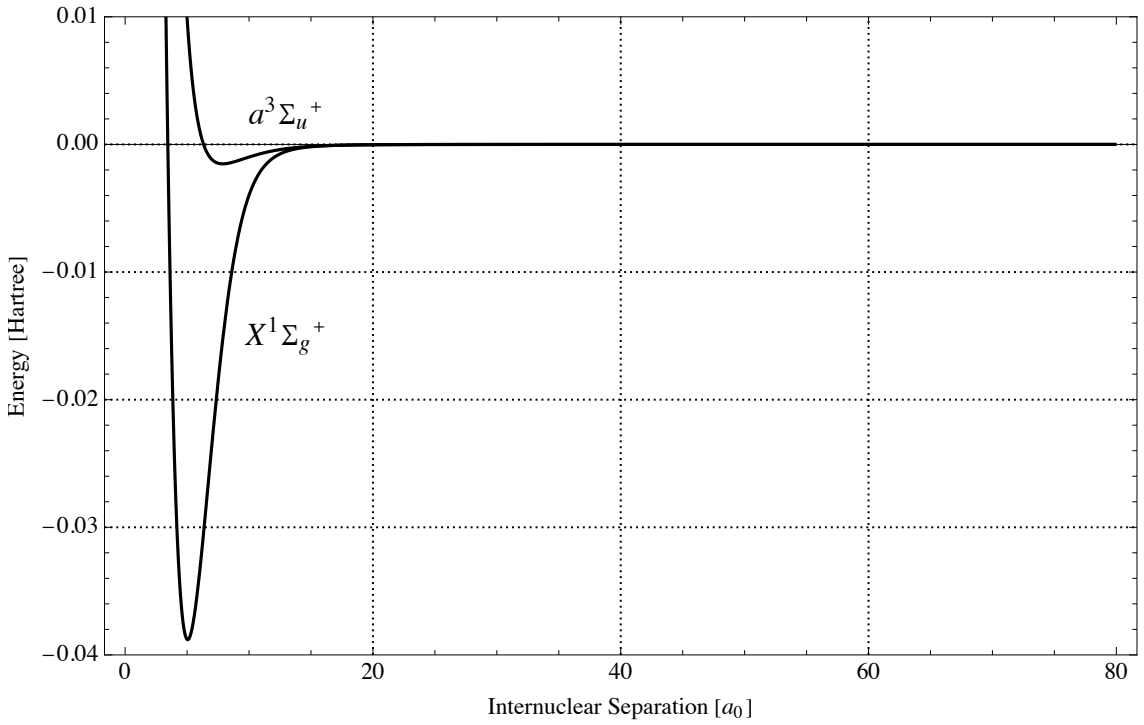

Figure 4-1: Ground state singlet $X^1\Sigma_g^+$ and lowest lying triplet $a^3\Sigma_u^+$ states for $^7Li_2$ [45] [44].

If $E > E^{thresh}$, then the channel is open, and a continuum of physical scattering solutions are accessible to the system. On the other hand, if $E < E^{thresh}$, the channel is closed and the wavefunction must vanish as $r \to \infty$. In the following sections, we will consider the latter of these cases (i.e., $E < E^{thresh}$), using QDT to calculate the bound states of this channel. This essentially boils down to separating the $^7Li_2$ interaction into three different regions, solving the radial Schrodinger equation in each, and matching the solutions to calculate relevant scattering observables.

4.3.1 Short-Range Region

At short-range (i.e., $r \leq 30\ a_0$), the deep wells of the Born-Oppenheimer potentials dominate Eq. (4.5). This means that we can describe the system at short-range with two uncoupled, second-order, ordinary differential equations.

$$\begin{aligned} \frac{d^2\psi_0}{dr^2} + \Big[V_0(r) - E\Big]\psi_0(r) = 0 \\ \frac{d^2\psi_1}{dr^2} + \Big[V_1(r) - E\Big]\psi_1(r) = 0 \end{aligned} \tag{4.9}$$

The solutions $\psi_0(r)$ and $\psi_1(r)$ are found by solving Eq. (4.9) numerically using *Mathematica*'s built-in differential equation solver (i.e., NDSolve function) with boundary conditions requiring that the wavefunctions, ψ_1 and ψ_0, vanish at $r = 0$ (in practice, at some small finite r) and their derivatives are small and finite. We match these two solutions and their derivatives, separately, to linear combinations of two linearly

independent solutions $\hat{f}(r)$ and $\hat{g}(r)$ of the long-range region at r_m.

$$\begin{aligned}\psi_\lambda(r_m) &= \hat{f}(r_m) - \tan(\pi\mu_\lambda)\hat{g}(r_m) \\ \psi'_\lambda(r_m) &= \hat{f}'(r_m) - \tan(\pi\mu_\lambda)\hat{g}'(r_m)\end{aligned} \tag{4.10}$$

Here, λ labels the total electronic spin quantum number S, μ_λ are the singlet and triplet quantum defects, and the distance r_m is chosen so that the channel is locally open and V_λ are well-approximated by V_{LR}. For alkali collisions, $r_m \approx 35 - 50\ a_0$. The quantities $\pi\mu_\lambda$ are the short-range phase shifts or the amount of phase that wavefunction accumulates in the singlet and triplet potential wells. Using Eq. (4.10), we arrive at the following expression for μ_λ,

$$\tan(\pi\mu_\lambda) = \frac{\hat{f}(r_m)Y_\lambda - \hat{f}'(r_m)}{\hat{g}(r_m)Y_\lambda - \hat{g}'(r_m)} \tag{4.11}$$

where $Y_\lambda = \frac{\psi'_\lambda(r_m)}{\psi_\lambda(r_m)}$ is the log-derivative of ψ_λ at the matching radius. Because the depths of the potentials at short-range are so much larger than $E^{collision}$, the quantum defects μ_λ are largely independent of the magnitude of the applied field or the collision energy as seen in Figure 4-2, and therefore, we will be performing calculations using an "energy independent frame transformation". In that approximation, we only need to tabulate the quantum defect at $E = B = 0$.

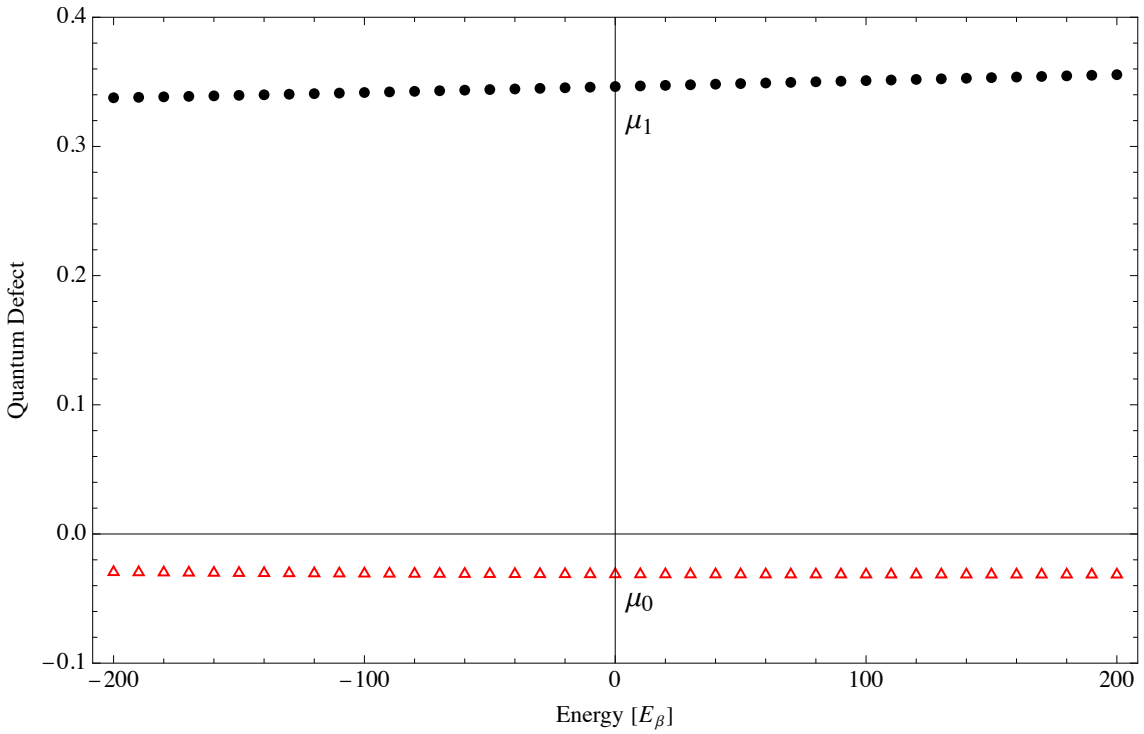

Figure 4-2: Singlet μ_0 and triplet μ_1 quantum defects for $^7Li_2$ as a function of the collision energy in units of van der Waals energy E_β. The solutions were matched at $r_m = 40\ a_0$.

At large r, the total electronic spin S is no longer a good quantum number, and the state of the system is not given by one of the molecular states $|S\ M_S\ I\ M_I\rangle$ but by the asymptotic channel $|a\rangle = (1,\ 1)$ (which is the eigenstate of Eq. (4.4) with the lowest energy eigenvalue). Therefore, to calculate the total short-range

reaction amplitude K^{sr}, we must to employ the following transformation,

$$K^{sr} = \sum_{\lambda} \langle a|\lambda\rangle \tan \pi\mu_{\lambda} \langle\lambda|a\rangle \tag{4.12}$$

where $|\lambda\rangle = |SM_S IM_I\rangle$. At zero-field, $|a\rangle = |\{1\ 1\ 1\ 1\}\rangle$ and Eqs. (4.12) becomes,

$$K^{sr} = \sum_{\lambda} P_{\lambda} \tan \pi\mu_{\lambda}. \tag{4.13}$$

4.3.2 Long-Range Region

In this region, the interaction between the two particles is given by Eq. (4.1) and the radial Schrodinger equation is

$$\frac{d^2\psi_{lr}}{dr^2} + \left[-\frac{C_6}{r^6} - \frac{C_8}{r^8} - \frac{C_{10}}{r^{10}} - E \right] \psi_{lr}(r) = 0 \tag{4.14}$$

where $E = E^{collision} - E^{thresh}$. The general solution to Eq. (4.14) is given by,

$$\psi_{lr}(r) = \hat{f}(r) - K^{sr}\hat{g}(r) \tag{4.15}$$

where $\hat{f}(r)$ and $\hat{g}(r)$ are two linearly independent solutions to Eq. (4.14) and K^{sr} is the total short-range reaction amplitude given by Eq. (4.12). We use Milne's phase amplitude method to construct the reference solutions $\hat{f}(r)$ and $\hat{g}(r)$:

$$\hat{f}(r) = \alpha(r) \sin\left(\int_{r_x}^{r} \alpha(r')^{-2} dr' + \phi \right) \tag{4.16}$$

$$\hat{g}(r) = -\alpha(r) \cos\left(\int_{r_x}^{r} \alpha(r')^{-2} dr' + \phi \right) \tag{4.17}$$

[41] [32]. Here, ϕ is a phase which ensures that Eqs. (4.16)-(4.17) remain linearly independent out to large r, where we have to match ψ_{lr} to solutions at $r \to \infty$. The amplitude function $\alpha(r)$ is found by solving the following differential equation,

$$\alpha(r)'' + k(r)^2\alpha(r) = \frac{1}{\alpha(r)^3} \tag{4.18}$$

where $k = \sqrt{E - V_{LR}}$, with WKB-like boundary conditions applied at $r = r_x$:

$$\alpha(r_x) = k(r_x)^{-1/2} \tag{4.19}$$

$$\alpha(r_x)' = \frac{d}{dr}\big(k(r)^{-1/2}\big)_{r=r_x}. \tag{4.20}$$

The selection of the radial distance r_x is somewhat arbitrary. All that is required is that $V_{LR}(r)$ is deep enough that our semi-classical boundary conditions are reasonable (i.e., that the potential varies slowly in comparison to the wavelength $\lambda = 2\pi/k$).

Selection of ϕ

The validity of the QDT calculation relies on the choice of the reference functions $\hat{f}(r)$ and $\hat{g}(r)$. In particular, we require that $\hat{f}(r)$ and $\hat{g}(r)$ remain linearly independent out to large r and thus, we want to find a value of ϕ in Eqs. (4.16) and (4.17) which guarantees their maximal linear independence. Following refs. [8] and [46], we determine this ϕ by allowing one of the reference functions to asymptotically coincide with a particular wave function at zero energy. This wave function is one of the zero-energy solutions of the $1/r^6$ term which dominates $V_{lr}(r)$. These two solutions χ_0^+ and χ_0^- are defined as

$$\chi_0^+(r) = \sqrt{r} J_{-\frac{1}{4}(2l+1)}(1/2r^2) \propto r^{l+1} \tag{4.21}$$

$$\chi_0^-(r) = \sqrt{r} J_{\frac{1}{4}(2l+1)}(1/2r^2) \propto r^{-l}. \tag{4.22}$$

where $J_\nu(x)$ is the Bessel function of the first kind [42]. Any zero-energy solution, therefore, is given by a superposition ofχ_0^+ and χ_0^-, including the reference wavefunctions of $\hat{f}(r)$ and $\hat{g}(r)$:

$$\begin{aligned} \hat{f}(r) &= A\chi_0^+(r) + B\chi_0^-(r) \\ \hat{g}(r) &= C\chi_0^+(r) + D\chi_0^-(r) \end{aligned} \tag{4.23}$$

where A, B, C, and D are coefficients determined by initial boundary conditions. However, as $r \to \infty$, χ_0^+ grows exponentially for $l \neq 0$ or linearly for $l = 0$, while χ_0^- quickly decays to zero for $l \neq 0$ or approaches a constant for $l = 0$. Thus, Eq. (4.23) will begin to approach χ_0^+ as r increases and therefore, $\hat{f}(r)$ and $\hat{g}(r)$ will be linearly dependent at large r, as both will be proportional to Eq. (4.21). This presents a problem because we require that $\hat{f}(r)$ and $\hat{g}(r)$ remain linearly independent out to large r. To mitigate this issue, we demand that $C = 0$ in Eq. (4.23) and $\hat{g}(r)$ coincides with χ_0^- at zero energy [46]. There is a unique value of ϕ that satisfies this condition and it can be found from the expression,

$$\tan\phi = -\frac{W\big(\chi_0^-(r), \hat{g}_{\phi=0}(r)\big)}{W\big(\chi_0^-(r), \hat{f}_{\phi=0}(r)\big)}\bigg|_{r=r_f} \tag{4.24}$$

where $W(x, y)$ is the Wronskian, given by $W(x, y) = xy' - x'y$, and r_f is an arbitrarily chosen separation distance at very large r [46]. For s-wave collisions, $r_f \sim 150\ a_0$ will suffice. Moreover, the calculation ϕ only needs to be done once at $E = 0$ and $B = 0$, since we are matching the reference functions to zero-energy solutions.

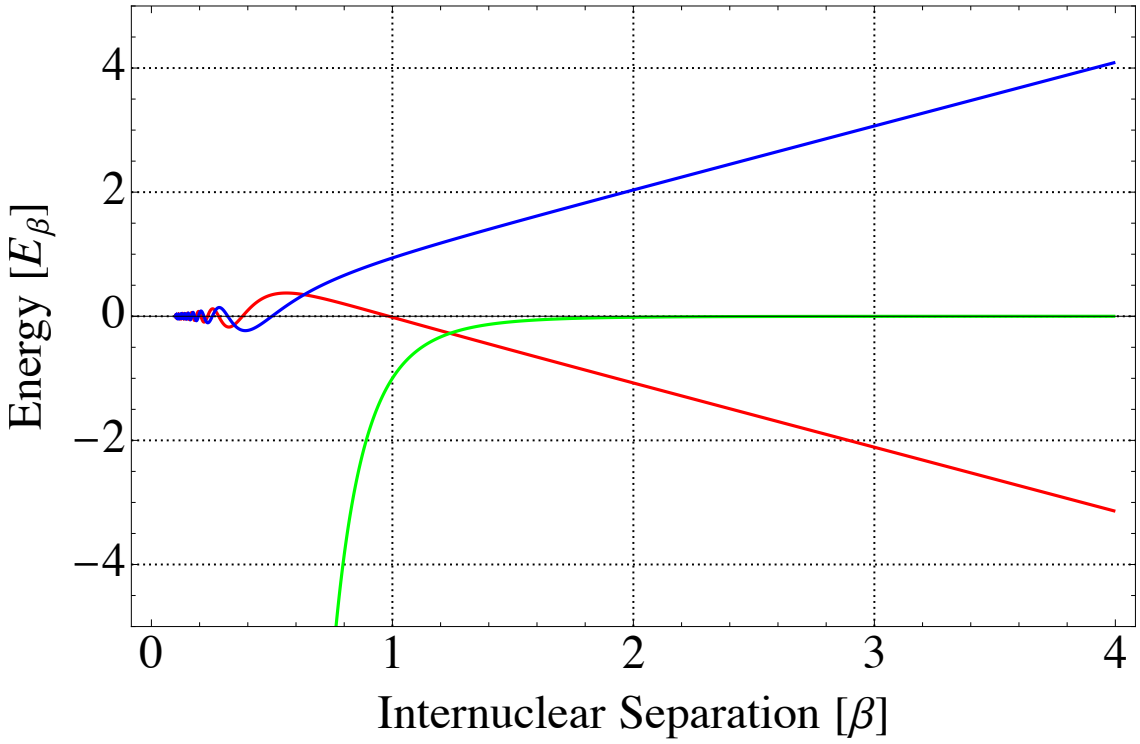

Figure 4-3: $\hat{f}(r)$ and $\hat{g}(r)$ with ϕ arbitrarily set to zero. The red curve corresponds to $\hat{f}(r)$, the blue to $\hat{g}(r)$, and the green to $V_{lr}(r)$. Notice that at large r, the solutions are linearly dependent and proportional to χ_0^+ beyond the range of the potential.

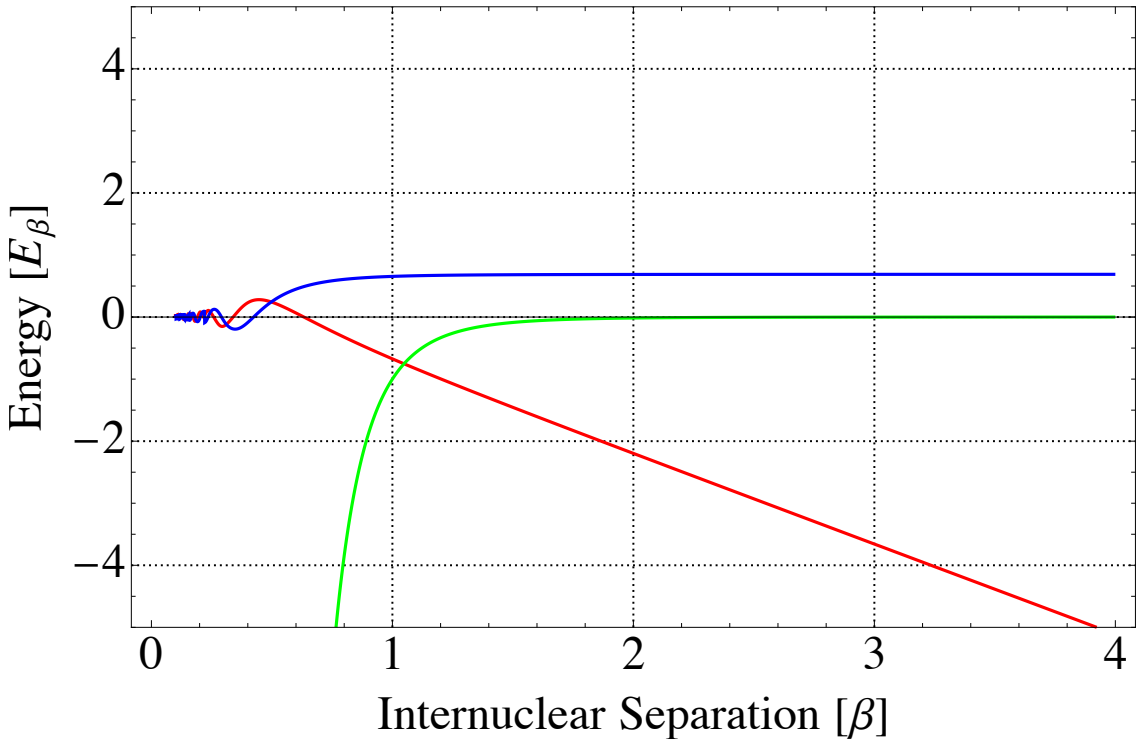

Figure 4-4: $\hat{f}(r)$ and $\hat{g}(r)$ with ϕ calculated using Eq. (4.24). The red curve corresponds to $\hat{f}(r)$, the blue to $\hat{g}(r)$, and the green to $V_{lr}(r)$. Notice that at large r, beyond the range of the potential, the solutions are linearly independent as $\hat{g}(r) \to \propto \chi_0^-$ and $\hat{f}(r) \to \propto \chi_0^+$.

4.3.3 Very Long-Range Region

Beyond r_f, the leading van der Waals term $-\frac{C_6}{r^6}$ in Eq. (4.1) is negligible, and the time-independent Schrodinger equation can be approximated by,

$$\frac{d^2\psi_{vlr}}{dr^2} - E\psi_{vlr}(r) = 0. \tag{4.25}$$

The solution $\psi_{lr}(r)$ depends on whether or not the interaction channel is open or closed as $r \to \infty$. If the channel is open, then the solution to Eq. (4.25) is a superposition of the phase-shifted, energy-normalized Riccati functions

$$f(r) = \sqrt{\frac{k}{\pi}} r j_l(kr + \eta) \tag{4.26}$$

and

$$g(r) = \sqrt{\frac{k}{\pi}} r n_l(kr + \eta) \tag{4.27}$$

where η is the phase accumulated in the long-range interaction region, $k = \sqrt{E}$ and $j_l(kr)$ and $n_l(kr)$ are spherical Bessel functions. Asymptotically, Eq. (4.26) and (4.27) approach,

$$f(r) \xrightarrow[r\to\infty]{} \frac{1}{\sqrt{k}} \sin\big(kr - l\pi/2 + \eta\big) \tag{4.28}$$

and

$$g(r) \xrightarrow[r\to\infty]{} -\frac{1}{\sqrt{k}} \cos\big(kr - l\pi/2 + \eta\big). \tag{4.29}$$

If the channel is closed, then $\psi_{lr}(r)$ must vanish as $r \to \infty$ and the solution is proportional to,

$$\chi^-(r) \propto e^{-\kappa r} \tag{4.30}$$

where $\kappa = \sqrt{|E|}$.

QDT Parameters

A collection of parameters connect the reference solutions $\hat{f}(r)$ and $\hat{g}(r)$ of the van der Waals region to the (physical) asymptotic solutions given by Eqs. (4.28)-(4.30). These parameters are analytical functions of energy, containing all the sensitive energy dependencies which arise from the passage from the high-energy short-range region to the low-energy long-range region [43]. We derive the expressions for these QDT parameters by matching a linear combination of $\hat{f}(r)$ and $\hat{g}(r)$ to a superposition of $f(r)$ and $g(r)$, if the channel open at large r, or to a decaying exponential, if the channel is closed asymptotically, at $r = r_f$.

Three of these parameters arise from matching the van der Waals reference functions to the energy-normalized, scattering solutions $f(r)$ and $g(r)$: $\mathcal{A}, \mathcal{G}$ and η. The first two of these, $\mathcal{A}$ and $\mathcal{G}$, are used to transform $\hat{f}(r)$ and $\hat{g}(r)$ into $f(r)$ and $g(r)$,

$$\begin{pmatrix} f \\ g \end{pmatrix} = \begin{pmatrix} \mathcal{A}^{1/2} & 0 \\ \mathcal{A}^{-1/2}\mathcal{G} & \mathcal{A}^{-1/2} \end{pmatrix} \begin{pmatrix} \hat{f} \\ \hat{g} \end{pmatrix}. \tag{4.31}$$

The parameter $\mathcal{A}$ is given by the expression,

$$\mathcal{A} = -\frac{W\big(f(r), \hat{g}(r)\big) - \tan\eta W\big(g(r), \hat{g}(r)\big)}{W\big(g(r), \hat{f}(r)\big) + \tan\eta W\big(f(r), \hat{f}(r)\big)}\bigg|_{r\to r_f} \tag{4.32}$$

where $k = \sqrt{E}$, and it is responsible for the energy-normalization $\hat{f}(r)$ and $\hat{g}(r)$ [46]. In V_{lr}, the van der Waals reference functions accumulate phase, and the parameter $\mathcal{G}$ accounts for the difference in this phases

$$\mathcal{G} = -\frac{W\big(g(r), \hat{g}(r)\big)}{W\big(g(r), \hat{f}(r)\big)}\bigg|_{r\to r_f} \tag{4.33}$$

[46]. The parameter η represents the asymptotic phase shift of Eqs. (4.28) and (4.29) from the spherical Bessel functions $j_l(kr)$ and $n_l(kr)$ which approach,

$$j_l(r) \xrightarrow[r\to\infty]{} \frac{\sin\big(kr - l\pi/2\big)}{kr} \tag{4.34}$$

and

$$n_l(r) \xrightarrow[r\to\infty]{} -\frac{\cos\big(kr - l\pi/2\big)}{kr}. \tag{4.35}$$

asymptotically. η is calculated by taking the arc tangent of a ratio of Wronskians that involve the large r limit of $\hat{f}$ and $\hat{g}$,

$$\tan\eta = \frac{W\big((kr)j_l, \hat{f}(r)\big)}{W\big((kr)n_l, \hat{g}(r)\big)}\bigg|_{r\to r_f} \tag{4.36}$$

[46].

If the channel is closed, the linear combination of $\hat{f}(r)$ and $\hat{g}(r)$ which characterizes the solution in the long-range interaction region must approach Eq. (4.30) as $r \to \infty$,

$$\chi^-(r) = \hat{f}(r)\sin\gamma + \hat{g}(r)\cos\gamma \xrightarrow{r\to\infty} \propto e^{-\kappa r}. \tag{4.37}$$

The parameter γ in Eq. (4.37) is the closed-channel counterpart of η and it determines the supposition of the reference functions $\hat{f}(r)$ and $\hat{g}(r)$ that vanishes at very large r. Taking the Wronskians of this expression with $\hat{f}(r)$ and $\hat{g}(r)$, we find that

$$\tan\gamma = -\frac{W\big(e^{-\kappa r}, \hat{g}(r)\big)}{W\big(e^{-\kappa r}, \hat{f}(r)\big)}\bigg|_{r\to r_f}. \tag{4.38}$$

The parameter γ can then be found by taking the arc tangent of Eq. (4.38).

Low-Energy Forms of QDT Parameters

As $E \to 0$, the QDT parameters approach the following simple forms [46]:

$$\mathcal{A}^{1/2} \to -(\bar{a}_l\sqrt{E})^{l+1/2} \tag{4.39}$$

$$\eta \to (-1)^{l+1}(\bar{a}_l\sqrt{E})^{2l+1} + \frac{3\pi\Gamma(l-3/2)}{32\Gamma(l+7/2)}E^2 \tag{4.40}$$

$$\mathcal{G} \to (-1)^{l+1}(\bar{a}_l\sqrt{E})^{4l+2} - \frac{E}{(2l+3)(2l-1)} \tag{4.41}$$

$$\gamma \to \begin{cases} \bar{a}_0\sqrt{|E|} & l=0 \\ \frac{E}{(2l+3)(2l-1)} & l>0 \end{cases} \tag{4.42}$$

where $\bar{a}_l$ is a generalized, standard scattering length given by,

$$\bar{a}_l = \Big(\frac{\pi 2^{-(2l+3/2)}}{\Gamma(l/2+5/4)\Gamma(l+1/2)}\Big)^{2/(2l+1)} \tag{4.43}$$

and $\Gamma(x)$ is the gamma function [42]. For an s-wave collision, with $l=0$, these forms become,

$$\mathcal{A}_{l=0}^{1/2} \to -(\bar{a}_0\sqrt{E})^{1/2} \tag{4.44}$$

$$\eta_{l=0} \to -\bar{a}_0\sqrt{E} \tag{4.45}$$

$$\mathcal{G}_{l=0} \to \left(\frac{1}{3} - \bar{a}_0^2\right)E \tag{4.46}$$

$$\gamma_{l=0} \to \bar{a}_0\sqrt{|E|} \tag{4.47}$$

to first order in E, with $\bar{a}_0 = 0.477989$.

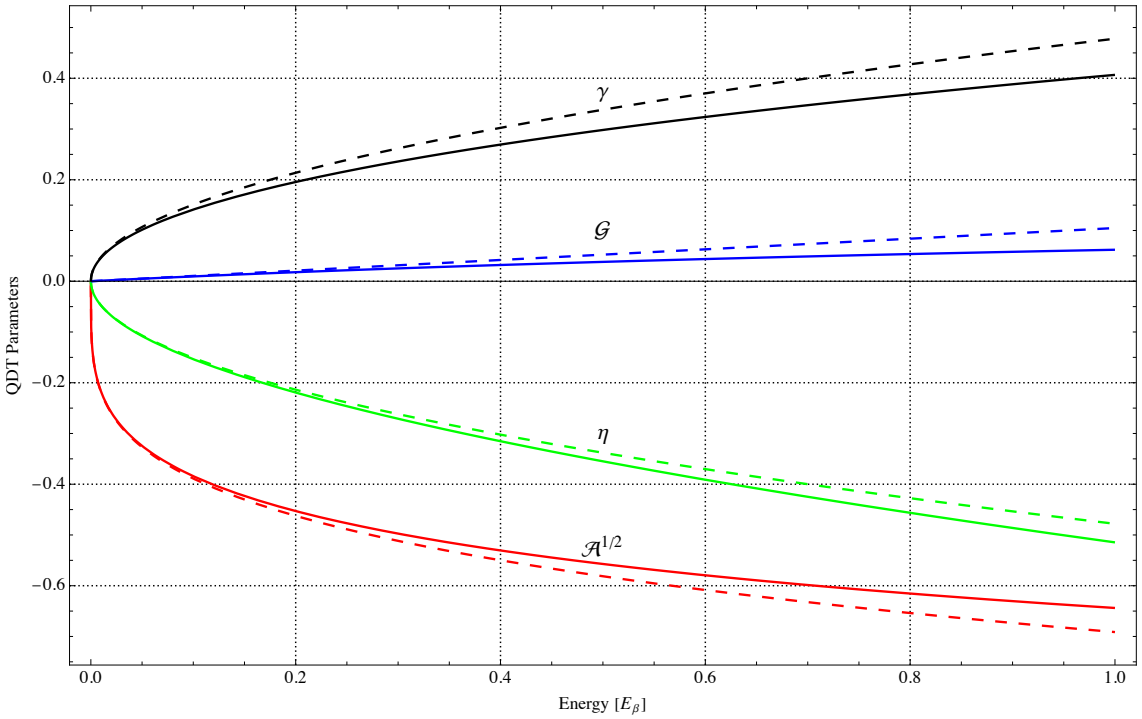

Figure 4-5: Curves of the MQDT parameters with respect to the collision energy in van der Waals units. The solid curves were generated using the full expressions for $\mathcal{A}$, $\mathcal{G}$, η, and γ, while the dashed lines correspond to the low-energy forms.

4.3.4 Bound State Calculation

If $E^{thresh} < E^{collision}$, then the channel wavefunction must asymptotically go to zero and be of the form Eq. (4.37) in the van der Waals region. However, $\psi_{lr}(r)$ is also given by Eq. (4.15). Matching these two expressions for the solution in the long-range region,

$$\hat{f}(r) - K^{sr}\hat{g}(r) = \hat{f}(r) + \cot\gamma\hat{g}(r) \tag{4.48}$$

we find that energies satisfying

$$K^{sr} + \cot\gamma = 0 \tag{4.49}$$

are bound states of the channel. Eq. (4.49) is evaluated a particular value of magnetic field B.

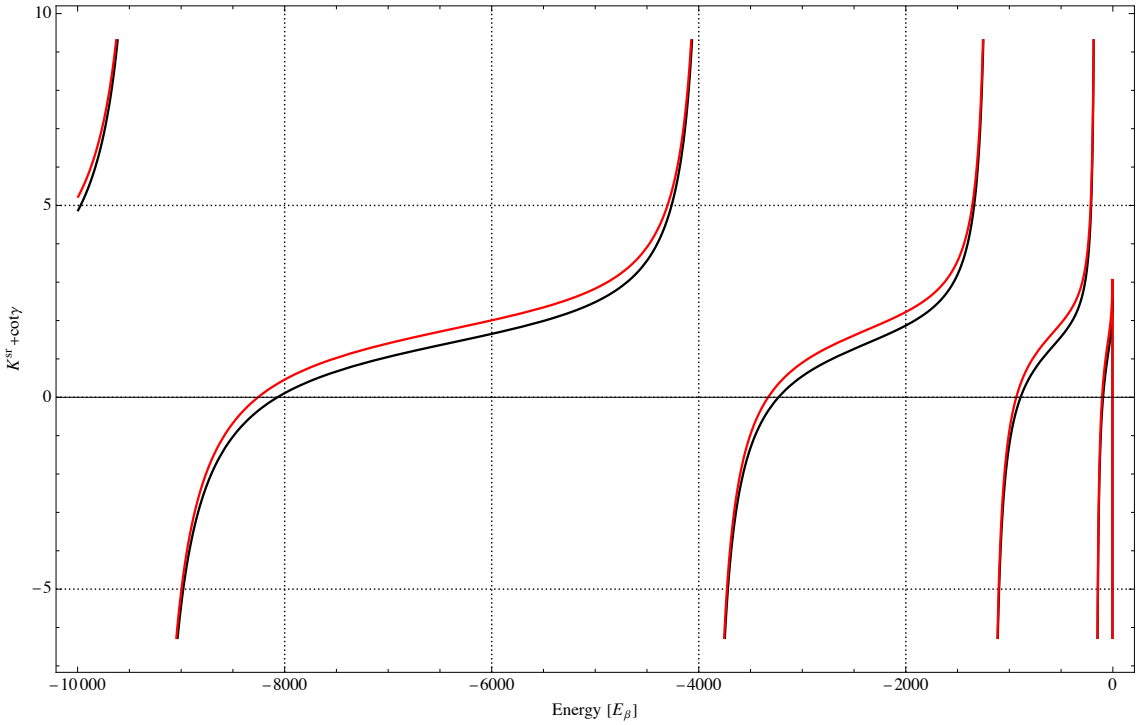

Figure 4-6: $K^{sr} + \cot(\gamma)$ versus energy in van der Waals units E_β for $B = 0$ Gauss (black curve) and $B = 1000$ Gauss (red curve). The zeros of the curves represent the bound states of the (1, 1) $^7Li_2$ collision channel.

4.4 Multi-Channel QDT

The QDT procedure outlined in the previous section can be generalized for multichannel problems to predict the number, position, and widths of Fano-Feshbach resonances with respect to the magnitude of an applied magnetic field B. To illustrate how this is done, we will consider an elastic, s-wave $^7Li_2$ collision in which the atoms enter and exit in the lowest lying channel with $M_F = 2$. The total Hamiltonian for this N-coupled channels problem is,

$$H = \frac{d^2}{dr^2} I + V(r) \tag{4.50}$$

where I is the $N \times N$ identity matrix and $V(r)$ the total potential which is given by Eq. (4.2). The wavefunction is expanded in the basis of scattering channels $\Phi_i(\Omega)$ that correspond to the internal states of the well-separated particles,

$$\psi(r, \Omega) = r^{-1} \sum_{i=1}^{N} \Phi_i(\Omega) \psi_i(r). \tag{4.51}$$

Here, Ω represents all the internal degrees of freedom and $\Phi_i(\Omega)$ are the eigenstates of Eq. (4.4) [46]. The index i labels the scattering channels and N is the total number of channels. For our current calculation, $N = 5$. The wavefunction satisfies a set of coupled radial Schrodinger equations,

$$\sum_{j=1}^{N} \left[-\frac{d^2}{dr^2} \delta_{ij} + V_{ij}(r) \right] \psi_j(r) = E_i \psi_i, \tag{4.52}$$

where δ_{ij} is the Kronecker delta function, $E_i = E - E_i^{thresh}$ is the asymptotic kinetic energy in the i^{th} channel, E_i^{thresh} is the threshold energy of the i^{th} channel, and E is the energy [46]. Just as in the previous section, Eq. (4.52) is cast in van der Waals units β for lengths and E_β for energies. We set the energy of the system at a constant just above the threshold of the lowest channel E_1^{thresh}:

$$E = E_1^{thresh} + \Delta E, \tag{4.53}$$

where $\Delta E = 10^{-15}$ Hartree is the collision energy, and the external magnetic field is allowed to vary. This means that only the lowest channel is open system; the other four are energetically inaccessible at large r.

The matrix $\Psi(r)$, with elements $\Psi_{ij}(r) = \psi_i^j(r)$ represents the set of physical scattering solutions [46]. Here i runs from 1 to N and j from 1 to N_P, where N_P is the number of asymptotically open channels. Hence, for our $^7\text{Li}_2$ problem, $\Psi(r)$ has dimensions of 5×1. Each element of $\Psi(r)$ must vanish at $r = 0$,

$$\Psi_{ij}(0) = 0, \tag{4.54}$$

and asymptotically must approach,

$$\Psi_{ij}(r) \xrightarrow[r\to\infty]{} \propto e^{-ik_i r}\delta_{ij} - e^{ik_i r} S_{ij}^{phys} \tag{4.55}$$

in each open channel i, or

$$\Psi_{ij}(r) \xrightarrow[r\to\infty]{} 0 \tag{4.56}$$

in each closed channel i [46]. In Eq. (4.55), $k_i = \sqrt{E_i}$ is the asymptotic wavenumber in the i^{th} channel and S^{phys} is the physical scattering matrix, which contains on the information necessary to compute the scattering observables, such as the total elastic cross section σ_{el}, and the resonance behavior [46]. In the following sections, we will demonstrate how S^{phys} is tabulated using QDT and compare this method to a full-closed coupling (FCC) calculation using a log-derivative propagator which solves the scattering problem exactly [26]. Appendix 6.1 outlines the algorithm behind this latter numerical method.

4.4.1 Elastic Scattering Calculation

In the multichannel generalization of QDT, the long-range parameters $\mathcal{A}, \mathcal{G}, \eta$, and γ, as well as the short range reaction amplitude K^{sr} which encapsulates the physics at small r, become matrices. The short-range reaction matrix K^{sr} is given by,

$$K^{sr} = \left(Y\hat{g} - \hat{g}'\right)^{-1}\left(Y\hat{f} - \hat{f}'\right). \tag{4.57}$$

Here $Y = \Psi^{-1}\Psi'$ is the log-derivative of the wavefunction $\Psi(r)$ at $r = r_m$ and $\hat{f}$, $\hat{g}$, $\hat{f}'$, and $\hat{g}'$ are diagonal matrices with elements:

$$\hat{f}_{ij} = \hat{f}_i(r_m)\delta_{ij} = \alpha_i(r_m)\sin\left(\int_{r_x}^{r_m} \alpha_i(r)^{-2}dr + \phi\right)\delta_{ij}, \tag{4.58}$$

$$\hat{g}_{ij} = \hat{g}_i(r_m)\delta_{ij} = \alpha_i(r_m) - \cos\left(\int_{r_x}^{r_m} \alpha_i(r)^{-2} dr + \phi\right)\delta_{ij}, \tag{4.59}$$

$$\hat{f}'_{ij} = \hat{f}'_i(r_m)\delta_{ij}, \tag{4.60}$$

and

$$\hat{g}'_{ij} = \hat{g}'_i(r_m)\delta_{ij}, \tag{4.61}$$

where $\alpha_i(r)$ is the Milne phase amplitude function for the i^{th} channel defined by,

$$\alpha_i(r)'' + k_i(r)^2\alpha(r) = \frac{1}{\alpha_i(r)^3} \tag{4.62}$$

where $k_i = \sqrt{E_i - V_{LR}}$ is the local wavenumber in each channel and $V_{LR}(r)$ is the long-range potential given by Eq. (4.1). The boundary conditions for Eq. (4.62) are,

$$\alpha_i(r_x) = k_i(r_x)^{-1/2} \tag{4.63}$$

and

$$\alpha_i(r_x)' = \frac{d}{dr}\big(k_i(r)^{-1/2}\big)_{r=r_x}. \tag{4.64}$$

The separation distances r_m and r_x need to be chosen so that all the channels are open, $V_\lambda(r_m) \approx V_{LR}(r_m)$, and $V_{LR}(r_x)$ needs to be deep enough that the potential is slowing varying with respect to the wavelength $\lambda_i = 2\pi/k_i$ in each channel. For our ^{7}Li$_2$, $r_m = 30\ a_0$ and $r_x = 7\ a_0$. Moreover, because we require that all of the channels are open at the matching radius r_m, K^{sr}, Y, $\hat{f}$, $\hat{g}$, $\hat{f}'$, and $\hat{g}'$ are $N \times N$ matrices. Eq. (4.57) is the exact expression for the short-range reaction matrix. However, since the interaction at small r is dominated by the deep potential wells of the Born-Oppenheimer potentials, K^{sr} is largely independent of energy and field. This means that K^{sr} does not need to be calculated at each value of field or energy and is well approximated by its form at $E = B = 0$. The value of K^{sr} at $r = r_m$ can also be estimated from the singlet and triplet quantum defects, μ_λ, calculated at zero energy using Eq. (4.11).

Energy-Independent Frame Transformation

At short separation distances, i.e., $r \lesssim 30\ a_0$, the interaction between the alkali atoms is dominated by the deep wells of the singlet $V_0(r)$ and triplet $V_1(r)$ molecular ground state potentials. Therefore, to a good approximation, any hyperfine or Zeeman interactions can be neglected and the atomic system can be described by a set of uncoupled equations,

$$\left(-\frac{d^2}{dr^2} + V_0(r) + E\right)\psi_0(r) = 0 \tag{4.65}$$

$$\left(-\frac{d^2}{dr^2} + V_1(r) + E\right)\psi_1(r) = 0. \tag{4.66}$$

To find the solutions $\psi_0(r)$ and $\psi_1(r)$, we numerically integrate Eqs. (4.65) and (4.66) out to r_m at energy $E = 0$. Then we match each solution to a linear combination of $\hat{f}(r)$ and $\hat{g}(r)$ at r_m to determine the singlet and triplet quantum defects μ_λ at zero energy using Eq. (4.11). However, at large r, the total electronic

spin S is no longer a good quantum number and the interaction between the particles is no longer diagonal in the molecular basis $|\lambda\rangle = |S\ M_S\ I\ M_I\rangle$. Thus, we use the frame-transformation formula,

$$K^{sr}_{i,i'} = \sum_{\lambda} \langle i|\lambda\rangle \tan(\pi\mu_\lambda) \langle \lambda|i'\rangle \tag{4.67}$$

to approximate the short-range reaction matrix K^{sr} in terms of the basis $|i\rangle$ in which the system is diagonal at large r [8]. In absence of an external magnetic field, this basis is the hyperfine basis, $|i\rangle = |\{f_1\ m_1\ f_2\ m_2\}\rangle$. However, if there is an applied field, then the interaction at large r includes a contribution from Zeeman effects, which are not diagonal in the hyperfine basis. Rather, to find the asymptotic dissociation channels, we diagonalize Eq. (4.4), then we rotate the short-range reaction matrix obtained from Eq. (4.67) into this new basis.

Long-Range Parameters

The long range parameters, $\mathcal{A}, \mathcal{G}$, and η, are $N_P \times N_P$ diagonal matrices, with elements,

$$\mathcal{A}_{ij} = \mathcal{A}_i \delta_{ij}, \tag{4.68}$$

$$\mathcal{G}_{ij} = \mathcal{G}_i \delta_{ij}, \tag{4.69}$$

and

$$\eta_{ij} = \eta_i \delta_{ij}, \tag{4.70}$$

where the terms $\mathcal{A}_i, \mathcal{G}_i$, and η_i are the QDT parameters of the i^{th} open channel and calculated from Eqs. (4.32), (4.33), and (4.36). The parameter γ is an $N_Q \times N_Q$ matrix, where N_Q is the number of closed channels, with elements

$$\gamma_{ij} = \gamma_i \delta_{ij}, \tag{4.71}$$

tabulated from Eq. (4.38). In practice, we do not calculate $\mathcal{A}_i, \mathcal{G}_i$, η_i, and γ_i at every value field and energy for each relevant collision channel. Rather, we construct the QDT parameters as functions of energy by evaluating Eqs. (4.32), (4.33), (4.36), and (4.36) on a cubic energy grid and interpolating the resulting data.

Calculating the Physical S-Matrix

After calculating the short-range reaction matrix K^{sr} and constructing the QDT parameter matrices, we can compute the physical scattering matrix S^{phys}, scattering length a, and elastic cross section σ_{el} in a few easy steps. First, we partition K^{sr} into blocks based on which channels are asymptotically open and closed:

$$K^{sr} = \begin{pmatrix} K^{sr}_{PP} & K^{sr}_{PQ} \\ K^{sr}_{QP} & K^{sr}_{QQ} \end{pmatrix}. \tag{4.72}$$

Then, we use the closed channel parameter γ to transform the $N \times N$ short-range reaction matrix into an $N_P \times N_P$ matrix using the formula,

$$\tilde{K} = K^{sr}_{PP} - K^{sr}_{PQ}(K^{sr}_{QQ} + \cot\gamma)^{-1}K^{sr}_{QP}. \tag{4.73}$$

[46]. This transformation is necessary because at large r, some of the collision channels are closed, and therefore, are not available as scattering channels for the system. However, $\tilde{K}$ is not the physical reaction matrix because it is not properly normalized with respect to energy. We normalize $\tilde{K}$ using the expression,

$$K = \mathcal{A}^{1/2}(\tilde{K}^{-1} + \mathcal{G})^{-1}\mathcal{A}^{1/2} \tag{4.74}$$

[46]. Finally, S^{phys} is determined from K and the long-range parameter η:

$$S^{phys} = e^{i\eta}\frac{I + iK}{I - iK}e^{i\eta}. \tag{4.75}$$

[46], and the scattering length for our $^7Li_2$ is tabulated from,

$$a = -\frac{1}{\sqrt{E}}\Big(\frac{\tan\eta_{11} + K_{11}}{1 - \tan\eta_{11}K_{11}}\Big) \tag{4.76}$$

where K_{11} and η_{11} the elements of K and η for the lowest interaction channel (these are the only elements of reaction matrix and η-matrix since this is the only open channel). At low energies, the QDT parameters approach the forms given in Eq. (4.44)-(4.46) and the scattering length is well-approximated by,

$$a \xrightarrow[E\to 0]{} \bar{a}_0(1 - \tilde{K}_{11}) \tag{4.77}$$

where $\tilde{K}_{11}$ is the element of $\tilde{K}$ for the lowest interaction channel (again for our current calculation, this is the only element of $\tilde{K}$ since there is only one open channel) and $\bar{a}_0$ is determined from Eq. (4.43) with $l = 0$. Note, that we do not use the low-energy form of γ to approximate $\cot\gamma$ in Eq. (4.73), since for each closed channel we evaluate γ at the asymptotic kinetic energies $E_i = E - E_i^{thresh}$ the channels. The total elastic cross section σ_{el} is then tabulated using the following expression,

$$\sigma_{el} \approx 8\pi a^2 \tag{4.78}$$

since the atoms are identical. Figure 4-7 shows σ_{el} plotted versus the magnetic field B for our $^7Li_2$ collision. The sharp peak near ~ 743 Gauss, indicates a Fano-Feshbach resonance, or that closed channel bound state crosses the energy threshold of the lowest channel at ~ 743 Gauss, leading the formation of an unstable lithium dimer. The elastic cross section also has zeros at about 130 and 560 Gauss. These features indicate there is zero probability that the atoms will collide at these two fields.

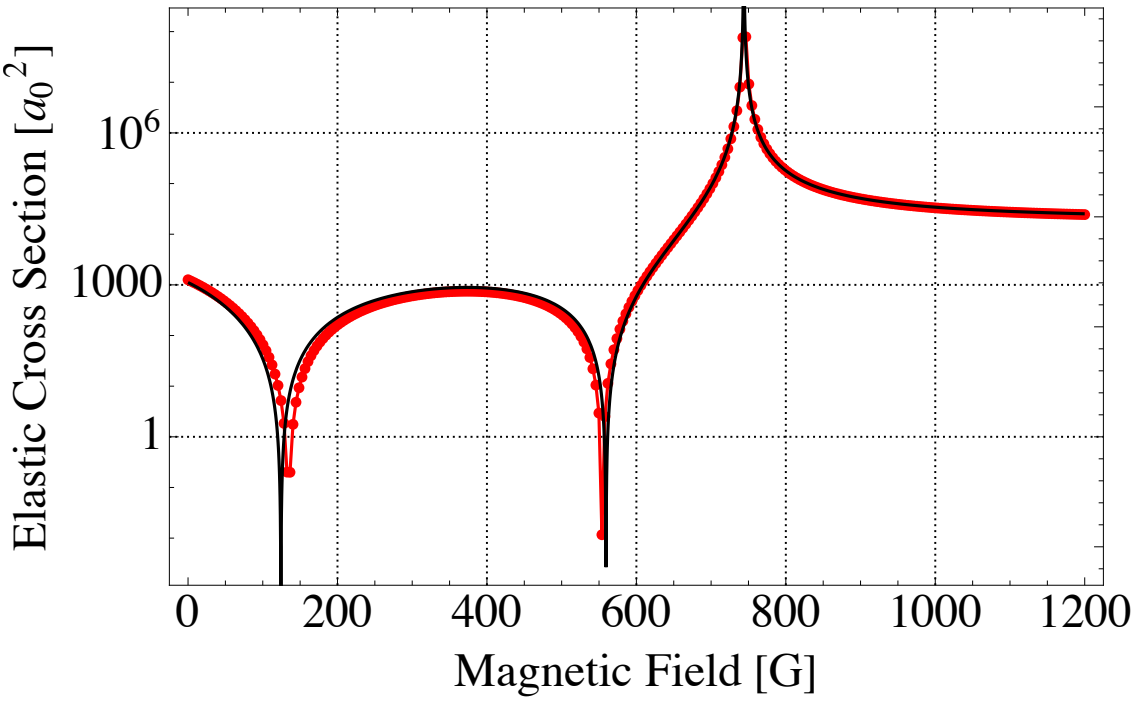

Figure 4-7: Elastic cross section for $^7Li_2$ in which the atoms enter and exit in the channel labeled (1, 1) in Figure 3-4. The black curve is from our frame transformation (FT) calculation and the red curve is from the FCC calculation.

Figure 4-7 also illustrates the success of our FT method at predicating the number, position, and widths of Fano-Feshbach resonances in an ultracold alkali collision. The FT calculation, indicated by the black curve in Figure 4-7, is able to almost exactly reproduce the resonance position of the FCC calculation, which is shown in red. However, the FT calculation is less accurate when it comes to the zeros of σ_{el}, in particular the zero near 130 Gauss. Table 4.1 summarizes the results from the FT and FCC calculations, as well as lists experimental values for the position of the resonance features.

	FT	FCC	Ref.[28]
Resonance position	743.7(4)	743.6(7)	737.69(2)
First zero	123.5(6)	129.6(2)	
Second zero	557.1(8)	553.9(3)	543.64(19)

Table 4.1: Elastic collision data for $^7Li_2$.

4.5 Success of QDT with a Frame Transformation

Given the relative success of our FT calculation for $^7Li_2$, we applied the method to other ultracold alkali systems to test its accuracy and reliability in predicting resonance features. In all of these calculations, we only consider elastic s-wave collisions between identical particles in which there is only one asymptotically open dissociation channel and four closed channels which contribute to the short-range physics. The results of these collisions are summarized in Figures 4-8, 4-9, 4-11, and 4-13, for $^6Li_2$, $^{23}Na_2$, $^{39}K_2$, and $^{87}Rb_2$, respectively. Overall, we found that accuracy of the frame transformation calculation depends on the

hyperfine/Zeeman splitting of the collisions channels. Recall that when we use Eq. (4.67) to approximate K^{sr}, we assume the hyperfine and Zeeman effects are so small compared to the depths of the $X^1\Sigma_g^+$ and $a^3\Sigma_u^+$ potentials that they can be neglected in the short-range region. This allows us to approximate the system by Eqs. (4.65) and (4.66) at small r and the short-range physics by the singlet and triplet quantum defects. In particular, we assume that the size of the hyperfine/Zeeman splitting of the collision channels at the matching radius r_m is negligible. However, in some alkali collisions, this assumption doesn't hold because the collision channels have already begun to shift and separate significantly by r_m and into the long-range region. This means that we need to include hyperfine and Zeeman effects in our calculation of K^{sr} for these alkali systems. Figures 3-1, 4-10, 4-12 and 4-14 show the splitting of the asymptotic dissociation channels for collisions of ^{6}Li, ^{23}Na, ^{39}K, and ^{87}Rb atoms versus magnetic field B. Notice that in the $^{39}K_2$ and $^6Li_2$ collisions, the size of the hyperfine/Zeeman splitting is comparable to that seen in the previous $^7Li_2$ problem and the FT approximation is able to reproduce the positions of Fano-Feshbach resonances to within 10 Gauss. Similarly in the $^{23}Na_2$ collision, where the hyperfine/Zeeman splitting is about twice as large as that seen in Figure 3-2, the FT method comes within 11 Gauss of the FCC calculation for the position of the Fano-Feshbach resonance. However, in the case of $^{87}Rb_2$, the frame transformation calculation fails to accurately produce the positions and widths of the four experimentally known resonances. Moreover, as Figure 4-14 illustrates, the hyperfine/Zeeman splitting in this systems is an order of magnitude larger than in the $^7Li_2$ collision.

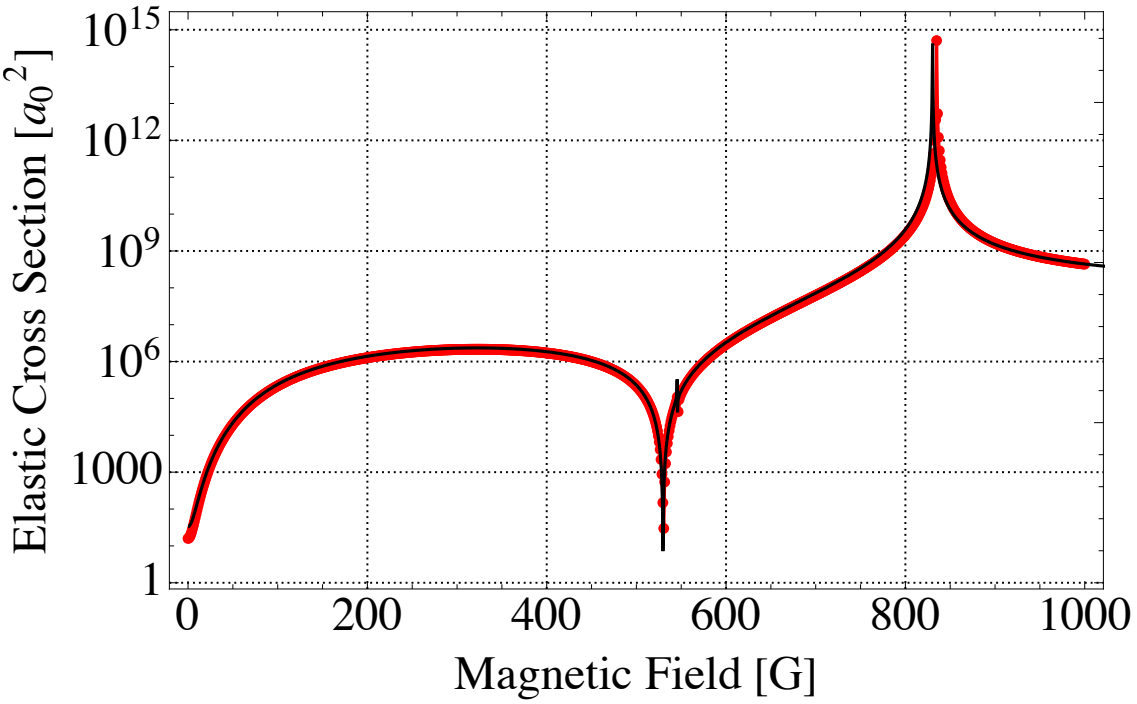

Figure 4-8: Elastic cross section for $^6Li_2$ in which the atoms enter and exit in the channel labeled (1, 2) in Figure 3-3. The black curve is from our FT calculation and the red curve is from the FCC calculation. Just as in the $^6Li^2$ collision, the FT method is able to reproduce the resonance features of the FCC calculation. There are two Feshbach resonances, a narrow one at $\sim$ 543 Gauss and a wide one at $\sim$ 828 Gauss, and one zero at $\sim$ 526 Gauss.

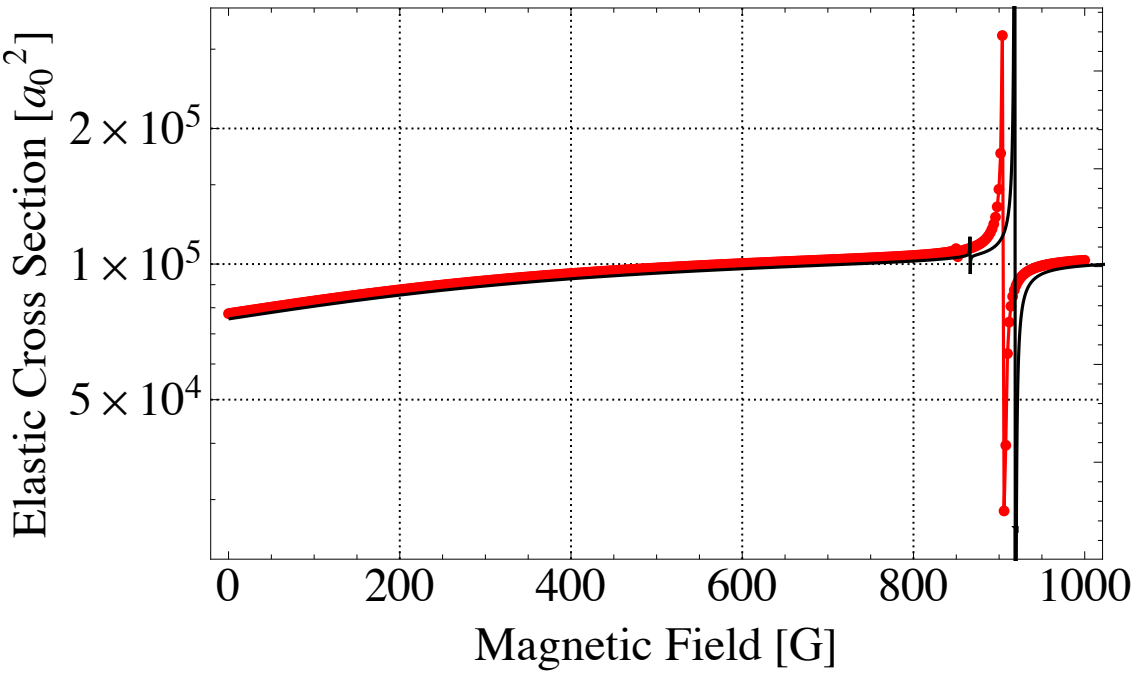

Figure 4-9: Elastic cross section for $^{23}Na_2$ in which the atoms enter and exit in the channel labeled (1, 1) in Figure 4-10). The black curve is from our FT calculation and the red curve is from the FCC calculation. There are two resonances; a narrow feature at about 860 Gauss and a wider one at $\sim$ 910 Gauss. Notice here, the FT calculation is not able to reproduce the resonance features as well had in the either of the lithium collisions. The difference in the narrow resonance is about 11 Gauss, with the FT calculation returning a value of 862.5(0) Gauss and the FCC calculation, 851.2(5) Gauss. For the wider resonance, the FT method returns a value of 916.5(0), about 11 Gauss from the FCC value of 905.0(7) Gauss.

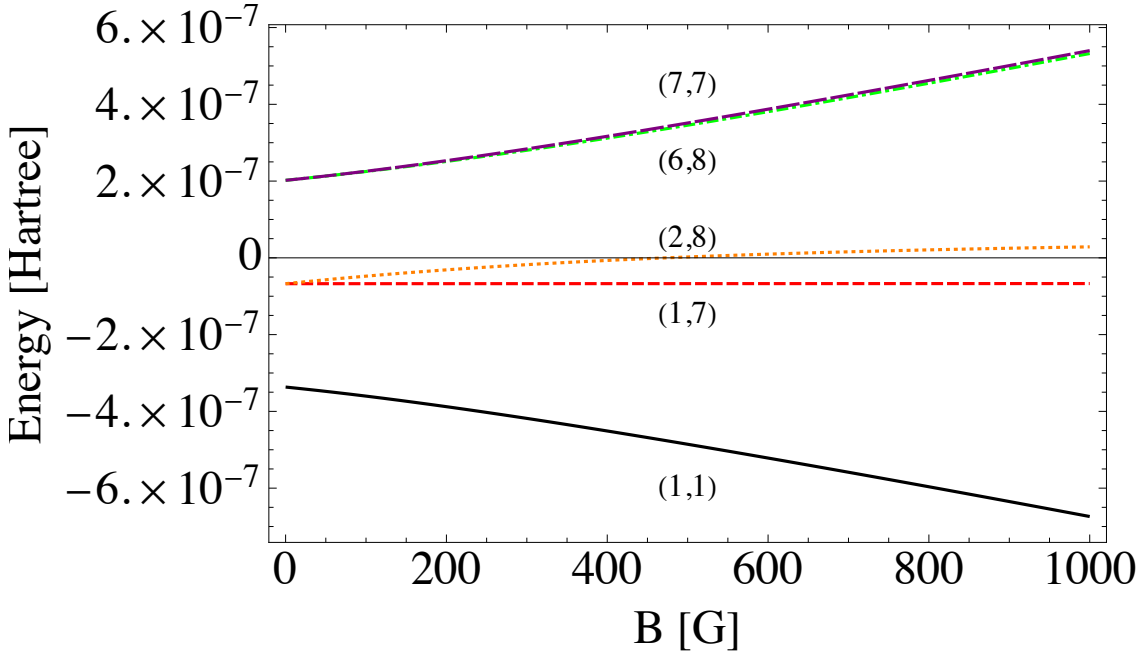

Figure 4-10: Zeeman/hyperfine splitting for $^{23}Na_2$ with $M_F = 2$. The labels on the curves correspond to the following symmetrized hyperfine kets at zero field: $(1,1) = |\{1\ 1\ 1\ 1\}\rangle$, $(1,7) = |\{1\ 1\ 2\ 1\}\rangle$, $(2,8) = |\{1\ 0\ 2\ 2\}\rangle$, $(6,8) = |\{2\ 0\ 2\ 2\}\rangle$, $(7,7) = |\{2\ 1\ 2\ 1\}\rangle$. Note that the splitting here is twice as large as in Figure 3-4.

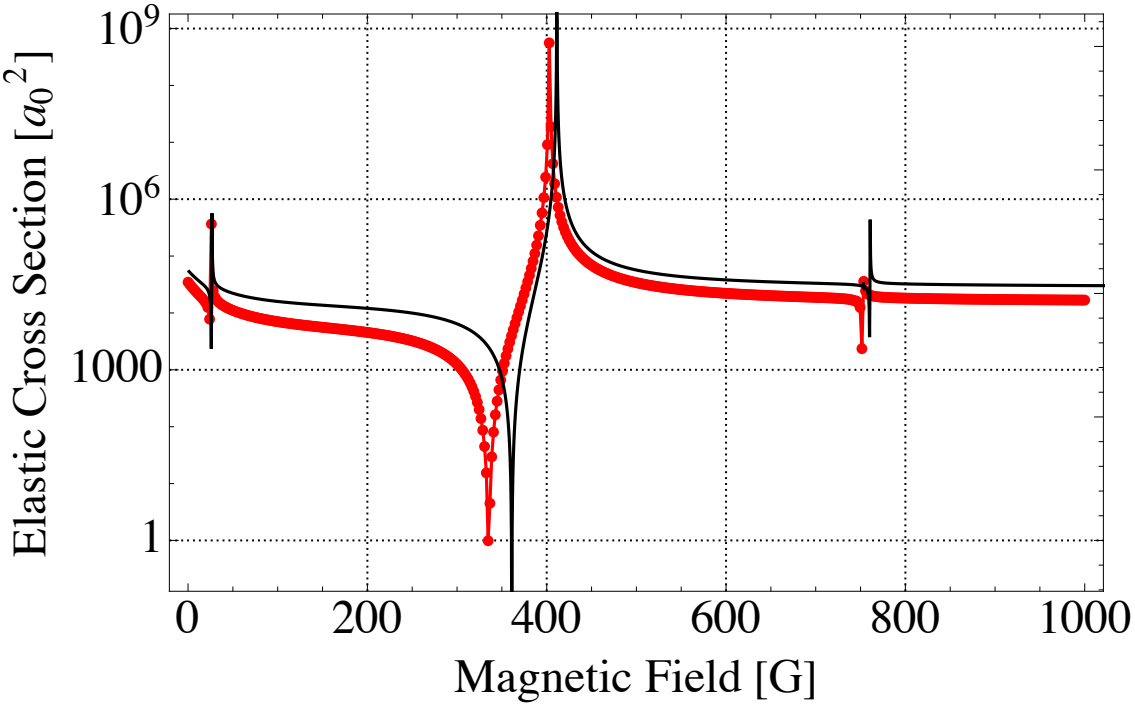

Figure 4-11: Elastic cross section for $^{39}K_2$ in which the atoms enter and exit in the channel labeled (1, 1) in Figure 4-12. The black curve is from our QDT calculation and the red curve is from the FCC calculation. There are four resonances, at about 25, 405, 750, and 755 Gauss and one zero at approximately 340 Gauss. Just as was observed in the $^{23}Na_2$ collision, the QDT method does not reproduce the resonance features of the FCC calculation as well as it had for the lithium collisions. In particular, there is about a 24 Gauss difference between the location of the zero; the FT calculation results in a value of 360.0(6) Gauss, while the FCC calculation returns 336.2(1) Gauss. However, the FT method is able to reproduce the first resonance almost exactly, resulting in a value of 24.9(5) Gauss which is only about 0.60 Gauss larger than the FCC value of 24.3(0) Gauss. For the other three Fano-Feshbach resonances, the FT calculation gives values which are about 10 Gauss higher than the corresponding FCC numbers: 411.7(5) Gauss (FT) and 403.0(9) Gauss (FCC); 753.1(3) Gauss (FT) and 744.0(8) Gauss (FCC); 760.2(4) Gauss (FT) and 752.0(2) Gauss (FCC).

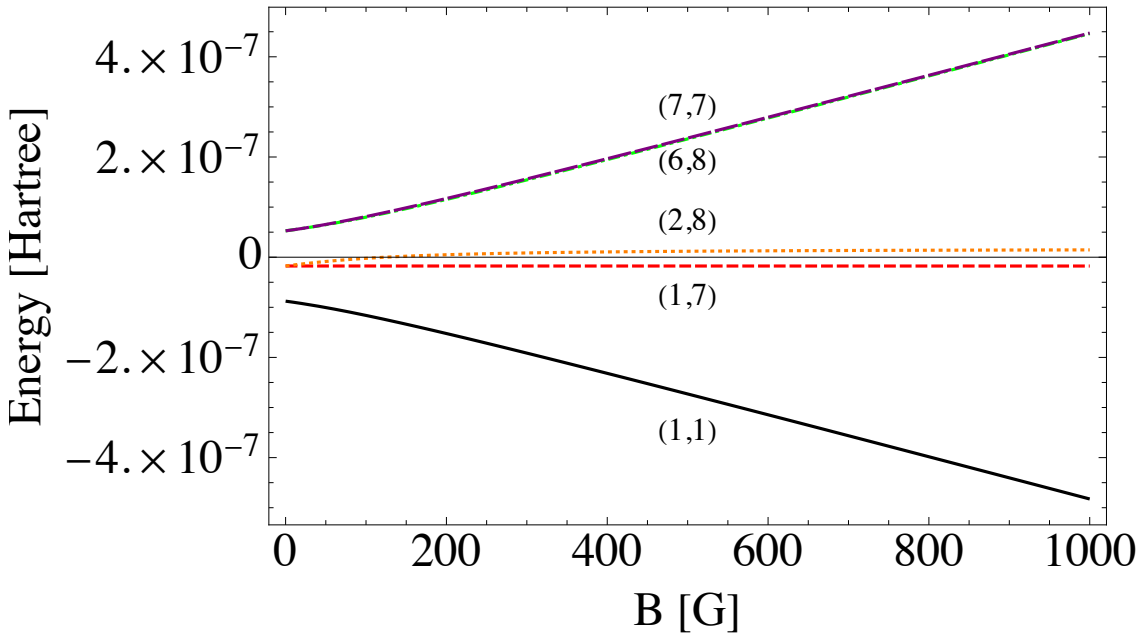

Figure 4-12: Zeeman/hyperfine splitting for $^{39}K_2$ with $M_F = 2$. The labels on the curves correspond to the following symmetrized hyperfine kets at zero field: $(1,1) = |\{1\ 1\ 1\ 1\}\rangle$, $(1,7) = |\{1\ 1\ 2\ 1\}\rangle$, $(2,8) = |\{1\ 0\ 2\ 2\}\rangle$, $(6,8) = |\{2\ 0\ 2\ 2\}\rangle$, $(7,7) = |\{2\ 1\ 2\ 1\}\rangle$. Here the splitting of the channels is comparable to that seen in Figure 3-4.

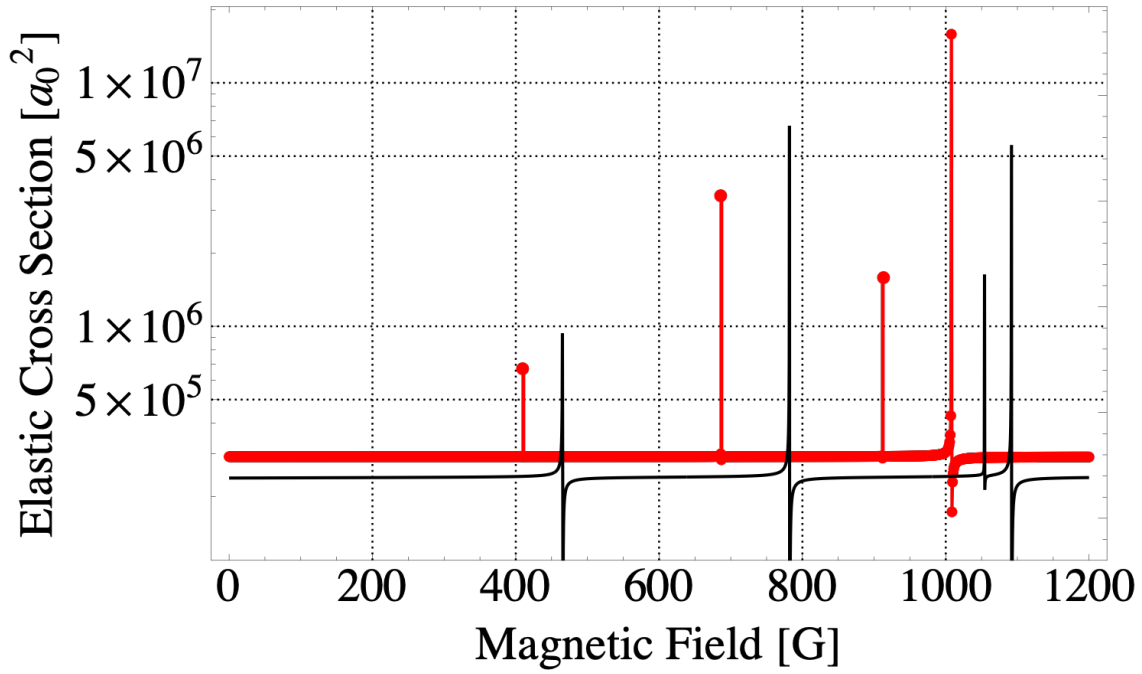

Figure 4-13: Elastic cross section for $^{87}Rb_2$ in which the atoms enter and exit in the channel labeled (1, 1) in Figure 4-14. The black curve is from our FT calculation and the red curve is from the FCC calculation. There are four resonances in this collision: (1) 406.23 Gauss with width 0.4 mG, 685.43 Gauss with width 17 mG, 911.74 Gauss with width 1.3 mG, and 1007.34 Gauss with width 170 mG [36]. The FCC calculation is able to reproduce these resonance features, but the FT calculation is not, giving values of 462.1(2) Gauss, 781.9(8) Gauss, 1054.2(2) Gauss, and 1090.1(6) Gauss.

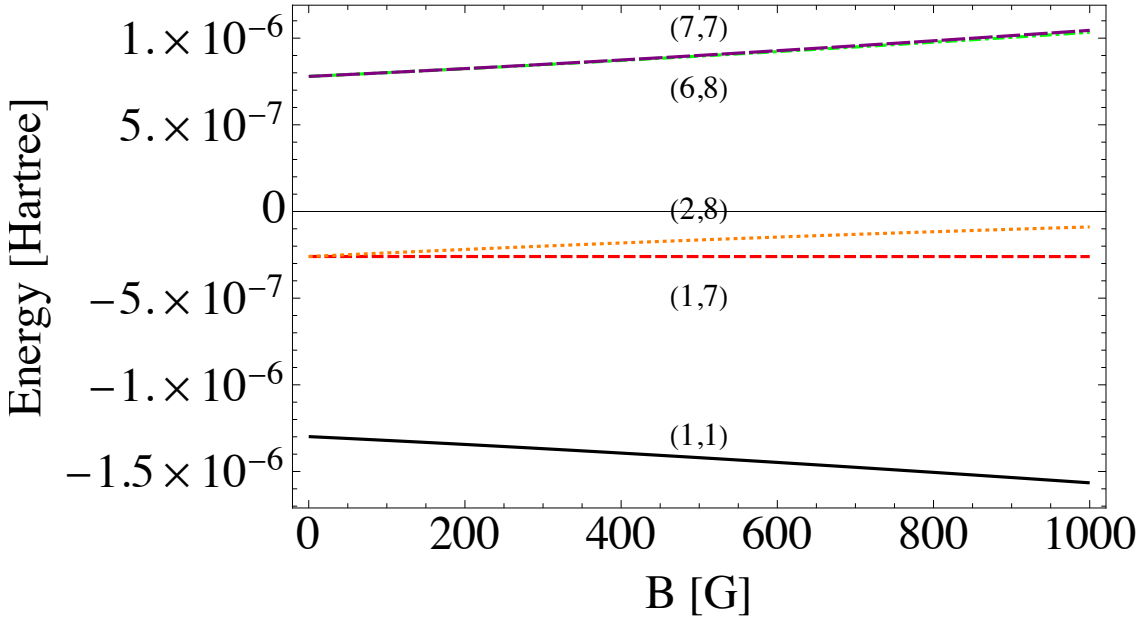

Figure 4-14: Zeeman/hyperfine splitting for $^{87}Rb_2$ with $M_F = 2$. The labels on the curves correspond to the following symmetrized hyperfine kets at zero field: $(1,1) = |\{1\ 1\ 1\ 1\}\rangle$, $(1,7) = |\{1\ 1\ 2\ 1\}\rangle$, $(2,8) = |\{1\ 0\ 2\ 2\}\rangle$, $(6,8) = |\{2\ 0\ 2\ 2\}\rangle$, $(7,7) = |\{2\ 1\ 2\ 1\}\rangle$. Notice that the splitting here is an order of magnitude larger than that seen in Figure 3-4.

Chapter 5

Conclusion

Here we have outlined a numerical method for predicting the resonance features in ultracold alkali collisions based on multichannel quantum defect theory with the addition of a frame transformation to approximate K^{sr}. We have found that the success of our FT calculation depends on the size of the hyperfine and Zeeman splitting of the collision channels in the area where the short- and long-range regions overlap. In systems where this effect is small, such as in the $^7Li_2$ or $^{39}K_2$ problems from the previous chapter, the FT method is able to reproduce the resonance features to within 10 Gauss. However, it fails in problems where this is not the case. Rather in such systems, like the $^{87}Rb_2$ collision in Chapter 4, it is necessary to include hyperfine and Zeeman terms in the short-range region and thus, in the calculation for the short-range reaction matrix. One could do this by first performing a full coupled channels calculation using the log-derivative propagator to find the log-derivative of wavefunction Y at the matching radius r_m and employing Eq. (4.57) to compute K^{sr}. The elastic cross section would then be tabulated from Eq. (4.72)-(4.76). Refs. [46] and [8] have used a similar procedure for collisions of rubidium and potassium atoms and found that it agreed with FCC calculations. Another solution for systems with large hyperfine/Zeeman splitting may be to employ another transformation—a rotation of the van der Waals reference solutions $\hat{f}(r)$ and $\hat{g}(r)$ like that suggested in ref. [20]. Also, it should be noted that here we have only considered elastic s-wave collisions. It would be interesting to see how well our current FT method is able to reproduce the resonance features of systems with that include higher partial waves or dipolar interactions between the atoms which couple channels with different values of total orbital angular momentum.

Chapter 6

Appendix

6.1 Log-Derivative Propagator

This appendix illustrates the algorithm behind Johnson's multichannel log-derivative propagator which was used to perform a full coupled-channels (FCC) calculation for the elastic cross section in our ultracold alkali collisions [26] [27]. This method solves the matrix Riccati equation

$$\mathbf{y}'(x) + \mathcal{V}(x) + \mathbf{y}^2(x) = 0, \tag{6.1}$$

where

$$\mathcal{V}(x) = \frac{2\mu}{\hbar^2}\big[E\mathbf{I} - \mathbf{V}(x) - \mathcal{E}\big]. \tag{6.2}$$

for the logarithmic derivative of the wave function defined as,

$$\mathbf{y}(x) = \mathbf{\Psi}'(x)\mathbf{\Psi}(x)^{-1}. \tag{6.3}$$

Here E is the total energy, μ is the reduced mass, $\mathbf{V}(x)$ is the symmetric potential matrix, including the angular momentum term, $\mathbf{I}$ is the identity matrix, and $\mathcal{E}$ is a diagonal matrix with elements $\mathcal{E}_{ij} = E_i^{thresh}\delta_{ij}$. The wavefunction $\mathbf{\Psi}(x)$ is a square matrix whose columns correspond to the linearly independent solutions of the one-dimensional matrix Schrodinger equation,

$$\left[\frac{d^2}{dx^2} + \mathcal{V}(x)\right]\mathbf{\Psi}(x) = 0 \tag{6.4}$$

with boundary conditions,

$$\mathbf{\Psi}(0) = 0 \tag{6.5}$$

and

$$\mathbf{\Psi}'(0) = \mathbf{I} \tag{6.6}$$

Eqs. (6.5) and (6.6) imply that the initial log-derivative matrix $\mathbf{y}_0 = \mathbf{y}(0)$ has infinite elements along the diagonal and $\mathbf{y}(x)$ is a symmetric matrix. In practice, the infinite elements of $\mathbf{y}(0)$ are set to finite but

very large numbers, such as 10^{20}; thus, we initially set

$$\mathbf{y}_0 = 10^{20}\mathbf{I}. \tag{6.7}$$

To numerically integrate Eq. (6.1) we employ the following algorithm:

$$\mathbf{y}_n = (\mathbf{I} + h\mathbf{y}_{n-1})^{-1}\mathbf{y}_{n-1} - \frac{h}{3}w_n\mathbf{u}_n \tag{6.8}$$

where n indexes the integration points, h is the spacing between integration points, and

$$\mathbf{u}_n = \begin{cases} \mathcal{V}(x_n), & n = 0, 2, 4, ..., N \\ \left[\mathbf{I} + (h^2/6)\mathcal{V}(x_n)\right]^{-1}\mathcal{V}(x_n), & n = 1, 3, 5, ..., N-1. \end{cases} \tag{6.9}$$

The weights, w_n, are given by,

$$w_n = \begin{cases} 1, & n = 0, N \\ 4, & n = 1, 3, 5, ..., N-1 \\ 2, & n = 2, 4, 6, ..., N-2. \end{cases} \tag{6.10}$$

It should be noted that only the log-derivative matrix at the final integration point, $\mathbf{y}(x_N) = \mathbf{y}_N$, is a good approximation to the actual value of $\mathbf{y}(x)$. We save one multiplication per step by solving for the quantity $\mathbf{z}_n = h\mathbf{y}_n$,

$$\mathbf{z}_n = \left(\mathbf{I} + \mathbf{z}_{n-1}\right)^{-1}\mathbf{z}_{n-1} - \frac{h^2}{3}w_n\mathbf{u}_n \tag{6.11}$$

and recover log-derivative matrix at the final integration point $\mathbf{y}_N$ with

$$\mathbf{y}_N = h^{-1}\mathbf{z}_N. \tag{6.12}$$

From Eq. (6.12), we construct the K-matrix at the final integration point x_N with,

$$\mathbf{K} = -\left(\mathbf{y}_N\mathbf{N}(x_N) - \mathbf{N}'(x_N)\right)^{-1} - \left(\mathbf{y}_N\mathbf{J}(x_N) - \mathbf{J}'(x_N)\right) \tag{6.13}$$

where $\mathbf{J}(x_N)$ and $\mathbf{N}(x_N)$ are diagonal matrices whose elements are made up of Riccati-Bessel functions [42]

$$\begin{aligned} \mathbf{J}(x_N)_{ij} &= k_i^{1/2} j_{l_i}(k_i x)\delta_{ij} \\ \mathbf{N}(x_N)_{ij} &= k_i^{1/2} n_{l_i}(k_i x)\delta_{ij} \end{aligned} \tag{6.14}$$

for open channels, and modified spherical Bessel functions of the first and third kinds [42]

$$\begin{aligned} \mathbf{J}(x_N)_{ij} &= (k_i x)^{1/2} I_{l_i+1/2}(k_i x)\delta_{ij} \\ \mathbf{N}(x_N)_{ij} &= (k_i x)^{1/2} K_{l_i+1/2}(k_i x)\delta_{ij} \end{aligned} \tag{6.15}$$

if the channel closed, where k_i is the channel wavenumber. Because the K-matrix contains elements from open (P) as well as closed (Q), in order to calculate the physical **S**-matrix, we partition Eq. (6.13) into blocks based on which channels are open or closed.

$$\mathbf{K} = \begin{pmatrix} \mathbf{K}_{PP} & \mathbf{K}_{PQ} \\ \mathbf{K}_{QP} & \mathbf{K}_{QQ} \end{pmatrix} \tag{6.16}$$

The **S**-matrix is then calculated from the open-open submatrix $\mathbf{K}_{PP}$,

$$\mathbf{S} = (\mathbf{I} + i\mathbf{K}_{PP})^{-1}(\mathbf{I} - i\mathbf{K}_{PP}). \tag{6.17}$$

Bibliography

[1] M. H. Anderson, J. R. Ensher, M. R. Matthews, C. E. Wieman, and E. A. Cornell. Observation of bose-einstein condensation in a dilute atomic vapor. *Science*, 269:198–201, 1995.

[2] E. Arimondo, M. Inguscio, and P. Violino. Experimental determinations of the hyperfine structure in the alkali atoms. *Rev. of Mod. Phys.*, 49:31–75, 1977.

[3] D. R. Bates and A. Damgaard. The calculation of the absolute strengths of spectral lines. *Phil. Trans. R. Soc. A*, 242, 1949.

[4] N. Bohr. The spectra of helium and hydrogen. *Nature*, 92:231–232, 1913.

[5] N. Bohr. On the quantum theory of radiation and the structure of the atom. *Phil. Mag.*, 30:394–415, 1915.

[6] C. C. Bradley, C. A. Sackett, J. J. Tollett, and R. G. Hulet. Evidence of bose-einstein condensation in an atomic gas with attractive interactions. *Phys. Rev. Letts.*, 75:1687–1690, 1995.

[7] A. Burgess and M. J. Seaton. A general formula for the calculation of atomic photoionization cross sections. *Mon. Not. R. Astron. Soc.*, 120, 1960.

[8] J. P. Burke. *Theoretical Investigation of Cold Alkali Atom Collisions.* Ph.D. thesis, University of Colorado at Boulder, 1999.

[9] J. P. Burke, C. H. Greene, and J. L. Bohn. Multichannel cold collisions: Simple dependences on energy and magnetic field. *Phys. Rev. Lett.*, 81, 1998.

[10] C. Chin, R. Grimm, P. S. Julienne, and E. Tiesinga. Feshbach resonances in ultracold gases. *Rev. Mod. Phys.*, 82:1225–1284, 2010.

[11] J. F. E Croft, A. O. G. Wallis, J. M. Hutson, and P. S. Julienne. Multichannel quantum defect theory for cold molecular collisions. *Phys. Rev. A*, 84:042703, 2011.

[12] K. B. Davis, M. O. Mewes, M. R. Andrews, N. J. van Druten, D. S. Durfee, D. M. Kurn, and W. Ketterle. Bose-einstein condensation in a gas of sodium atoms. *Phys. Rev. Letts.*, 75:3969–3973, 1995.

[13] B. DeMarco, J. L. Bohn, J. P. Burke, M. Holland, and D. S. Jin. Measurement of p-wave threshold law using evaporatively cooled fermionic atoms. *Phys. Rev. Lett.*, 82:4208–4211, 1999.

[14] S. Falke, H. Knockel, J. Friebe, M. Riedmann, E. Tiemann, and C. Lisdat. Potassium ground-state scattering parameters and born-oppenheimer potentials from molecular spectroscopy. *Phys. Rev. A*, 78:012503, 2008.

[15] U. Fano. Quantum defect theory for l uncoupling in h_2 as an example of channel-interaction treatment. *Phys. Rev. A*, 2:353, 1970.

[16] U. Fano. Unified treatment of perturbed series, continuous spectra and collisions. *J. Opt. Soc.*, 65: 979, 1975.

[17] U. Fano and A. R. P. Rau. *Atomic Collisions and Spectra*. Academic Press, 1986.

[18] H. Friedrich. *Scattering Theory*. Springer, 2013.

[19] M. Gailitis. Some features of the threshold behavior of the cross sections for excitation of hydrogen by electrons due to the existence of a linear stark effect in hydrogen. *Sov. Phys. JETP*, 17:1107–1110, 1963.

[20] C. H. Greene and S. Watanabe. Atomic polarizability in negative-ion photodetachment. *Phys. Rev. A*, 22:158–169, 1980.

[21] C. H. Greene, U. Fano, and G. Strinati. General form of the quantum-defect theory. *Phys. Rev. A*, 19:1485–1509, 1979.

[22] C. H. Greene, A. R. P. Rau, and U. Fano. General form of the quantum-defect theory ii. *Phys. Rev. A*, 26:2441–2459, 1982.

[23] D. Griffiths. *Introduction to Quantum Mechanics*. Cambridge University Press, 2017.

[24] D. R. Hartree. The wave mechanics of an atom with a non-coulomb central field. *Proc. Camb. Phil. Soc.*, 24, 1928.

[25] W. Heisenberg. Uber quantentheoretische umdeutung kinematischer und mechanischer beziehungen. *Z. Phys.*, 33:879–893, 1925.

[26] B. R. Johnson. The multichannel log-derivative method for scattering calculations. *J. Comput. Phys.*, 13:445–449, 1973.

[27] B. R. Johnson. The renormalized numerov method applied to calculating bound states of the coupled-channel schroedinger equation. *J. Chem. Phys.*, 69:4678–4688, 1978.

[28] P. S. Julienne and J. M. Hutson. Contrasting the wide feshbach resonance in ^{6}li and $_7$li. *Phys. Rev. A*, 89:052715, 2014.

[29] Ch. Jungen. Quantum defect theory for molecules. In J. S. Briggs, H. Kleinpoppen, and H. O. Lutz, editors, *Fundamental Processes of Atomic Dynamics*, pages 79–103. Springer US, 1988.

[30] W. Ketterle and N. J. van Druten. Evaporative cooling of trapped atoms. *Adv. At., Mol., Opt. Phys.*, 37:181–236, 1997.

[31] S. Knoop, T. Schuster, R. Scelle, A. Trautmann, J. Appmeier, M. K. Oberthaler, E. Tiesinga, and E. Tiemann. Feshbach spectroscopy and analysis of the interaction potentials of ultracold sodium. *Phys. Rev. A*, 83:042704, 2011.

[32] H. J. Korsch and H. Laurent. Milne's differential equation and numerical solutions of the schrodinger equation. *J. Phys. B. Atom. Mol. Phys.*, 14, 1981.

[33] H. Kragh. *Niels Bohr and the Quantum Atom: The Bohr Model of Atomic Structure 1913-1925*. Oxford Scholarship Online, 2012.

[34] L. D. Landau and E. M. Lifschitz. *Quantum Mechanics Nonrelativistic Theory*. Pergamon Press, 1977.

[35] H. Margenau. Van der waals forces. *Reviews of Modern Physics*, 11:1–35, 1939.

[36] A. Marte, T. Volz, J. Schuster, S. Durr, G. Rempe, E. G. M. van Kempen, and B. J. Vehaar. Feshbach resonances in rubidium 87: Precision measurement and analysis. *Phys. Rev. Lett.*, 89:283202, 2002.

[37] W. I. McAlexander. *Collisional Interactions in an Ultracold Lithium Gas*. Ph.D. thesis, Rice University, August 2000.

[38] H. J. Metcalf and P. van der Straten. *Laser Cooling and Trapping*. Springer, 1999.

[39] F. H. Mies. A multichannel quantum defect theory analysis of diatomic predissociation and inelastic atomic scattering. *J. Chem. Phys.*, 80, 1984.

[40] F. H. Mies and M. Raoult. Analysi of threshold effects in ultracold atomic collision. *Phys. Rev. A*, 62:012708, 2000.

[41] W. E. Milne. The numerical determination of characteristic numbers. *Phys. Rev.*, 35:863–867, 1930.

[42] F. W. J. Oliver, D. W. Lozier, R. F. Boisevert, and C. W. Clark. *NIST Handbook of Mathematical Functions*. Cambridge University Press, 2010.

[43] A. R. P. Rau. Relationships between the parameters of quantum-defect theory. *Phys. Rev. A.*, 38, 1988.

[44] R. J. Le Roy and N. S. Dattani. A dpf data analysis yields accurate analytic potentials for li_2 ($a^3\sigma_u^+$) and li_2 ($1^3\sigma_g^+$) that incorporate 3-state mixing near the $1^3\sigma_g^+$ state asymptote. *J. Mol. Spectrosc.*, 268:199–210, 2011.

[45] R. J. Le Roy, N. S. Dattani, J. A. Coxon, A. J. Ross, P. Crozet, and C. Linton. Accurate analytic potentials for li_2 ($x^1\sigma_g^+$) and li_2 ($a^1\sigma_u^+$) from 2 to 90 å, and the radiative lifetime of li(2p). *J. Chem. Phys.*, 131:204309, 2009.

[46] B. P. Ruzic, C. H. Greene, and J. L. Bohn. Quantum defect theory for high-partial-wave cold collision. *Phys. Rev. A*, 87, 2013.

[47] F. Schreck, L. Khaykovich, K. L. Corwin, G. Ferrari, T. Bourdel, J. Cubizolles, and C. Salomon. Quasipure bose-einstein condensate immersed in a fermi sea. *Phys. Rev. Lett.*, 87:080403, 2001.

[48] E. Schrodinger. Versuch zur modellmassigen deutung des terms der scharfen nebenserien. *Z. Phys.*, 4, 1921.

[49] E. Schrodinger. Die wassertoffahnlichen spektren vom standpunkte der polarisierbarkeit des atomrumpfes. *Ann. Phys.*, 77:43–70, 1925.

[50] A. Sommerfeld. Zur quantentheorie der spektrallinien. *Ann. Phys.*, 356:1–94, 1916.

[51] H. T. C. Stoof, J. M. V. A. Koelman, and B. J. Verhaar. Spin-exchange and dipole relaxation rates in atomic hydrogen: Rigorous and simplified calculations. *Phys. Rev. B*, 38:4688–4697, 1987.

[52] C. Strauss, T. Takekoshi, F. Lang, K. Winkler, R. Grimm, J. Hecker Denschlag, and E. Tiemann. Hyperfine, rotational, and vibration structure of the $a^3\sigma_u^+$ state of $^{87}\mathrm{rb}_2$. *Phys. Rev. A*, 82:052514, 2010.

[53] J. R. Taylor. *Scattering Theory: The Quantum Theory of Nonrelativistic Collisions.* Dover Publications, 2006.

[54] A. G. Truscott, K. E. Strecker, W. I. McAlexander, G. B. Partridge, and R. G. Hulet. Observation of fermi pressure in a gas of trapped atoms. *Science*, 291:2570–2572, 2001.